

COOLING AND DETECTABILITY OF NEUTRON STARS

Sachiko Tsuruta

Smithsonian Astrophysical Observatory, Cambridge, Mass.;
Physics Department, Columbia University, New York, N.Y.;
and Institute for Space Studies,
Goddard Space Flight Center, NASA, New York, N.Y.

and

A.G.W. Cameron
Institute for Space Studies,
Goddard Space Flight Center, NASA
New York, New York

GPO PRICE \$ _____

CFSTI PRICE(S) \$ _____

Hard copy (HC) 3.00

Microfiche (MF) 1.65

ff 653 July 65

18198

ABSTRACT

Surface properties, temperature effects, cooling behavior, and observability of neutron stars have been studied. For this purpose the opacity of the surface layers is calculated both for a pure iron and a pure magnesium composition. It is found that the non-degenerate layers are only a few meters thick and in no case exceed 1% of the stellar radius. The star cools mainly through neutrino emission when $T \geq 1 \sim 4 \times 10^8$ °K, but at lower temperatures the cooling is primarily through electromagnetic radiation. The neutrino cooling mechanisms included were the neutrino plasma process, the URCA process, and the neutrino bremsstrahlung process. The cooling behavior is quite complicated. The rate of cooling generally depends on mass, nuclear potential, and surface composition, among which the dependence on mass is the most significant. It will be hard to observe low mass neutron stars due to fast cooling rates. However,

~~NASA Offices and Research Centers~~

Abstract cont on back of this case!

N67-18198

(ACCESSION NUMBER)

(THRU)

(PAGES)

(CODE)

(NASA CR OR TMX OR AD NUMBER)

(CATEGORY)

medium and high mass stars should still have temperatures exceeding about 2×10^6 °K on the surface for times of the order of 10^3 to 10^5 years. Hence it should not be impossible to observe massive neutron stars relatively close to us, if there is no x-ray emission of larger flux coming from the surrounding region.

Author

INTRODUCTION

From studies of nucleosynthesis and stellar evolution it appears likely that the remnants of some supernova explosions will probably contain a central core of highly condensed matter of the order of nuclear density whose main composition is neutrons, and of surrounding envelopes of ejected material which are expanding continuously (Arnett 1966, Cameron 1959 a, b, 1965a, Chiu 1964, Colgate and White 1965, Zwicky 1938, 1939, 1958). The central core, which may become as hot as $\sim 10^{11}$ °K at the peak, will cool down to $\sim 10^9$ °K within $\sim 10^{-5}$ sec or so (Chiu 1964), due to the extremely high rates of neutrino cooling. Whether the remnant, if a stable neutron star, will ever be detectable depends critically on the cooling behavior of the neutron star itself and on physical conditions in the ejected envelope.

When the first, crude, information on the recently

1961

discovered galactic x-ray sources became available (Bowyer, Byram, Chubb and Friedman 1964 a, Giacconi, Gursky, Paolini and Rossi 1962, 1963, Fisher and Meyerott 1964), it was tempting to identify these x-ray sources with neutron stars, for a neutron star of photospheric temperature $T_e \sim 10^6$ to 10^7 °K would emit soft x-rays with peak near $30 \sim 3\text{\AA}$ if it can be regarded as a black body. The first series of cooling calculations showed that neutron stars of this range of temperature can be sufficiently luminous and last sufficiently long to be consistent with the early observational data (Chiu and Salpeter 1964, Morton 1964, Tsuruta 1964). In the meantime, possible cooling mechanisms have been reexamined and some faster cooling mechanisms have been proposed (Bahcall and Wolf 1965 a, c, Finzi 1965a, Tsuruta and Cameron 1965 a). The results of our latest calculations (whose details are given in this paper) indicate that a neutron star with $T_e \sim 10^7$ °K will cool too fast, 1 day to 10 years (for models of different mass), to be detected as x-ray sources, but that if $T_e \sim 2 \times 10^6$ °K, the medium and high mass stars will last sufficiently long for detection ($\sim 10^{3 \sim 5}$ years). The conclusion is that the cooling rate alone does not exclude the possibility that some neutron stars will be detectable, provided that the thermal soft x-ray emission exceeds the nonthermal background from the ejected envelope.

If we look at a bare neutron star in a vacuum, there would be several characteristic features which could be checked. For instance, a neutron star (of radius ~ 10 km) should appear to be a point source, and the x-ray spectrum from it should approximate that of blackbody radiation. A lunar occultation measurement conducted by Boyer, Byram, Chubb and Friedman (1964 b) showed that the source in the Crab Nebula has a diameter of about one light year. Clark (1965) and others reported that the same source emits a significant x-ray flux in ~ 30 keV region, which is inconsistent with the spectrum of a blackbody radiation from a surface of a few million degrees. The MIT and American Science and Engineering group and the Livermore group reported that the spectrum of the strongest x-ray source in Scorpius is inconsistent with the hypothesis of blackbody radiation (Giacconi, Gursky and Waters 1965, Chodil, Jopson, Mark, Seward and Swift 1965). These observational results seem to indicate that the observed x-rays from some sources do not consist alone of blackbody radiation from a neutron star. However, we cannot conclude that these results are evidence against the existence of neutron stars.

One of us (Cameron 1965 b) suggested that a possible model of an x-ray source may be a vibrating neutron star with an associated magnetosphere and surrounding hot

gas clouds. (Also, see Finzi 1965 b). The central neutron core may emit thermal x-rays and the surrounding area may emit non-thermal x-rays (either synchrotron radiation or bremsstrahlung). The question of whether the observed x-rays are thermal, non-thermal, or a mixture will require more extensive observations. Some of the recent experiments quoted above only suggest that the thermal component is not the main contribution to the observed x-rays, and that the effects from the surrounding envelopes are dominant. The problem of whether we can distinguish between the thermal component from the neutron star and the non-thermal components from the surrounding area will be considered in the last section of this paper. As long as there is a possibility that neutron stars are related to the galactic x-ray source, directly or indirectly, the study of neutron stars will continue to be of astronomical importance, as well as of fundamental importance in general relativistic physics.

In our earlier paper (Tsuruta and Cameron 1966) properties of neutron stars which are independent of temperature were studied. Here we discuss some thermal properties of these neutron stars. For this purpose six typical models have been chosen from our first paper. Three of these are

based on the V_{β} type of nuclear potential, and the other three are based on the V_{γ} type of potential. The different types of potential correspond to different assumptions about the possible nuclear forces which will govern the interactions between the constituent baryons. Among the three models for each type of potential, one is of low mass at the low density base of the principal mass peak, one is half-way up the peak, and the other is near the top of the peak. The characteristic properties of these models are listed in Table 1. Each model is designated by its potential type and approximate mass value. It has been suggested that a model with density $\rho > 8 \rho_{\text{nucl}}$ (ρ_{nucl} is the nuclear density = 3.7×10^{14} gm/cm³) is unreliable (Bahcall and Wolf 1965 a, b) due to the uncertainty in high energy physics. Our model ($V_{\beta}, 1M_{\odot}$) is denser than this critical limit. However, all other models lie roughly within the limit of validity and the general conclusions deduced from these models are expected to be reasonably reliable.

Typical models of quite different mass value and nuclear potential have been chosen in order to avoid as far as possible the danger of drawing general conclusions from limited assumptions. The main approach was, therefore, to set upper and lower limits which define the range where the most probable models of neutron stars would lie.

In the following sections the surface properties of neutron stars will be studied first, the cooling and related calculations will be presented, and finally the problem of detectability will be discussed.

ENVELOPE STRUCTURE EQUATIONS

The structure equations for the outer layers of a neutron star are:

$$(1) \quad \frac{dP_r}{dr} = - \frac{[P_r/c^2 + \rho(r)]G(4\pi r^3 P_r/c^2 + M_r)}{r(r - 2M_r G/c^2)}$$

$$(2) \quad \frac{dM_r}{dr} = 4\pi r^2 \rho(r)$$

For radiative equilibrium or electron conduction:

$$(3) \quad \frac{dT_r}{dr} = - \frac{3}{4ac} \frac{\kappa(r) \rho(r)}{T_r^3} \frac{L}{4\pi r^2}$$

For convective equilibrium:

$$(4) \quad \frac{dT_r}{dr} = \left(1 - \frac{1}{\Gamma}\right) \frac{T_r}{P_r} \frac{dP_r}{dr}$$

where M_r , T_r , P_r , $\rho(r)$ and $\kappa(r)$ are the mass, temperature, pressure, density and opacity at a distance r from the center, L is the total luminosity of the star, G is the constant of gravitation, a is Stefan's radiation constant, c is the velocity of light, and Γ is the ratio of the specific heats c_p/c_v . The assumption was made that the star is spherically symmetric and in hydrostatic equilibrium and that there is no

energy generation or sinks in the envelope. The general relativistic expressions are used in the hydrostatic equations (1) and (2) because the general relativistic effects are quite important even near the surface for some of the denser stars (Tsuruta and Cameron 1966).

Near the surface, the above equations are more easily integrated in electronic computers if they are expressed in logarithmic form, and it is better to use pressure as an independent variable because the pressure gradient is quite high near the photosphere of neutron stars. Then Eqs. (1)-(3) can be expressed as:

$$(5) \quad \frac{d(\ln r)}{d(\ln P_r)} = - \exp (\ln P_r + \ln A - \ln B - \ln G - \ln D)$$

$$(6) \quad \frac{d(\ln M_r)}{d(\ln P_r)} = - \exp (3 \ln r - \ln M_r + \ln \left(\frac{4\pi}{G}\right) + \ln \rho(r) + \ln P_r + \ln A - \ln B - \ln D)$$

$$(7) \quad \frac{d(\ln T_r)}{d(\ln P_r)} = \exp [\ln (3/16\pi acG) + \ln (r) + \ln P(r) + \ln L - 4 \ln T - \ln r + \ln P_r + \ln A - \ln B - \ln D]$$

where

$$A = \exp (\ln r) - \exp (\ln 2 + \ln M_r - 2 \ln c + \ln G)$$

$$(8) \quad B = \exp (\ln \rho(r)) + \exp (\ln P_r - 2 \ln c)$$

$$D = \exp (\ln M_r) + \exp (\ln 4\pi + 3 \ln r + \ln P_r - 2 \ln c)$$

The equation of state in non-degenerate layers is

$$(9) \quad P = \left(\frac{1}{\mu_e} + \frac{1}{\mu_{ion}} \right) \frac{k \rho T}{H} + \frac{1}{3} a T^4$$

where the first term is the gas pressure and the last term is the radiation pressure. In degenerate envelopes, all pressures except the degenerate pressure of electrons are negligible and the following equation for degenerate electron gases is applicable:

$$(10) \quad \begin{aligned} P &= A f(\chi); & \rho &= n \mu_e H = B \chi^3, & \chi &= P_F / m_e c \\ f(\chi) &= \chi(2\chi^2 - 3)(\chi^2 + 1)^{\frac{1}{2}} + 3 \sinh^{-1} \chi \\ A &= \pi m_e^4 c^5 / (3h^3) = 6.01 \times 10^{22}, & B &= 8\pi m_e^3 c^3 \mu_e H / 3h^3 = 9.82 \times 10^5 \mu_e. \end{aligned}$$

μ_e and μ_{ion} are defined as

$$(11) \quad \begin{aligned} \mu_e &= \left[\sum_k A_k n(A_k, Z_k) \right] / \left[\sum_i Z_i n(A_i, Z_i) \right] \\ \mu_{ion} &= \left[\sum_k A_k n(A_k, Z_k) \right] / \left[\sum_i n(A_i, Z_i) \right] \end{aligned}$$

where $n(A_i, Z_i)$ is the number density of the nucleus i of mass number A_i and atomic number Z_i , H is the proton mass, and the remaining notation is conventional. The equilibrium composition of matter as found by Tsuruta and Cameron (1965b) was used. In the envelopes of neutron stars the equation of state is relatively simple as shown above, but the behavior of the opacity is quite complicated. For this reason, the opacity is treated separately in the next section. Generally,

great care has to be taken in evaluating Γ if the envelopes are in convective equilibrium. However, as is shown later, convection appears to play no role in neutron stars.

To obtain a proper boundary condition at the surface, it was assumed that the ordinary theory of stellar atmospheres would apply in the atmospheric layers above the surface of neutron stars, provided that general relativity effects are correctly taken into account in some of the denser models. The surface of the star is defined as the point where the actual temperature is equal to the effective temperature T_e (the temperature of the black body which would radiate the same flux as the star itself). Then the total luminosity of the star L is expressed as

$$(12) \quad L = 4\pi\sigma R^2 T_e^4,$$

σ is Stefan's constant.

If we assume that the opacity is independent of both height and wave length in the atmosphere but that it has the constant value determined at the photosphere, the theory of radiative transfer in stellar atmospheres leads us to the following simple relation:

$$(13) \quad P_{ph} = \int_0^{\tau_s} \frac{g(P_{ph}, \rho_{ph})}{\kappa(\rho_{ph}, T_e)} d\tau = \frac{2}{3} \frac{g(P_{ph}, \rho_{ph})}{\kappa(\rho_{ph}, T_e)}$$

where τ_s is the optical depth at the surface, (ρ_{ph}, T_e) is the

opacity at the photosphere and the general relativistic form of $g(P_{\text{ph}}, \rho_{\text{ph}})$ is:

$$(14) \quad g = \frac{GM}{R^2} \left(\frac{P_{\text{ph}}}{\rho_{\text{ph}} c^2} + 1 \right) \left(1 + \frac{4\pi R^3 P_{\text{ph}}}{Mc^2} \right) \left(1 - \frac{2GM}{Rc^2} \right)^{-1}.$$

The subscript ph stands for the value of the respective variable at the photosphere. Noting that the mass content and the thickness of the atmosphere of neutron stars are negligible, the radius and the gravitational mass of the cold models of neutron stars can be used for R and M above. Then equations (9), (13) and (14) evaluated at the photosphere give us sufficient boundary conditions at the surface of a neutron star of surface temperature T_e .

OPACITY

The total opacity κ in a neutron star can be expressed as

$$(15) \quad \frac{1}{\kappa} = \frac{1}{\kappa_R} + \frac{1}{\kappa_C}$$

where κ_R and κ_C are the radiative and conductive opacity, respectively. Radiative opacity is due to the various processes of atomic and molecular absorption, emission, and scattering of radiation in which electrons play the major role. The relative importance of these processes depends strongly on the temperature-density combination. For instance, in matter of high temperature and of relatively low

density, electron scattering is dominant, while in the region of intermediate density and temperature the various photoelectric effects are the most important. In degenerate matter of high density, electron conduction is the most efficient mechanism. The major processes of atomic absorption are the bound-free, free-free, and bound-bound processes. Excited electrons emit photons in the inverse processes. The scattering processes are Thomson scattering if $T \leq 5 \times 10^8$ K and Compton scattering for higher temperatures.

The opacity generally depends on density and temperature in quite a complicated way. In recent years, various extensive tables based on detailed computations have been published which give the absorption coefficient for many different compositions and for a large number of points in the temperature-density diagram. The most accurate method of obtaining opacities at present appears to be through use of the computer code for opacities constructed by A.N.Cox and his colleagues of the Los Alamos Scientific Laboratory (Cox, 1961), which includes most of the possible major processes contributing to opacity, and this code was kindly made available for our calculations. It includes bound-free and free-free absorption, electron scattering (both Thomson and Compton scattering), negative ion absorption

and electron conduction. The bound-free absorption depends on the equilibrium number of electrons which are bound in the various atomic states. When the ionization of one element is completed, no more bound-free absorption due to that element can occur. For high densities the effect of degeneracy is taken into account in all but the electron scattering term. At low densities and low temperatures not all electrons are ionized. An ionization code was used in conjunction with the opacity code in these regions to calculate the degree of ionization, the partial pressure of electrons, and the number of free electrons in the opacity calculations.

At temperatures above about 5×10^7 °K, almost all elements are ionized. The existing tables are used to obtain absorption cross sections for various kinds of processes. The electron scattering term is obtained for the non-degenerate case, and pair production of electrons and positrons is not considered. Therefore, the opacity is independent of density but dependent on temperature in the high temperature region where Compton scattering is dominant. Different approximations are applied for different degrees of degeneracy to evaluate the conductive opacity.

Values of the opacity were calculated for a pure iron

composition and a pure magnesium composition, in the range of temperature from $10^{3.7}$ °K to 10^{10} °K, and of density from $10^{-4.3}$ gm/cm³ to 10^{14} gm/cm³. The reason for these particular choices of composition is explained in the next section. Opacities at densities higher than 10^{14} gm/cm³ have not been included because degeneracy sets in at densities far below this. Calculations at temperatures higher than 10^{10} °K has not been carried out because the assumptions of nondegenerate electron scattering and no electron-positron pair creation cause serious errors there. Also, neutron stars of temperature higher than this are of no interest to us because they would cool too quickly. The case $T_e < 10^{3.7}$ °K and $\rho < 10^{-4.3}$ gm/cm³ was not included because the opacity code did not work in these low temperature, low density regions.

Results obtained are plotted in Figure 1. The solid curves represent the opacity of iron 56 as a function of density at different temperatures, while the dashed curves represent the same for magnesium 24. The opacity shows quite a complicated dependence on density and temperature in the region $\rho \leq 10^6$ gm/cm³ and $T \leq 10^8$ °K, where the transition from electron scattering or electron conduction to bound-free opacity occurs. The almost straight horizontal lines for $T \geq 10^9$ °K and $\rho \leq 10^6$ gm/cm³ are due to Compton scattering. The almost straight lines of negative slope in the region

of high density are an indication that electron conduction is the dominant factor in the transport of energy there. We can assume that degeneracy starts as soon as the opacity in Figure 1 starts to follow one of these straight negatively sloping lines. The opacities ($\ln\kappa$) thus obtained have been stored as an input deck of cards in the form of a two-dimensional table corresponding to given $\ln T$ and $\ln \rho$ combinations, for later use.

The results from the opacity code calculations were checked in the various asymptotic regions of density and temperature, using simpler, analytic approximations. In the region where photoelectric effects are dominant, the Kramers opacity formulae (see, for instance, Schwarzschild 1958) were used. The opacity due to electron scattering was checked through the equations given by Sampson (1959). In order to check the opacity in the region of electron conduction the relations in Schatzman (1958) were used. The agreement was quite satisfactory. It turned out that the neglect of degeneracy and electron-positron pair creation in the formulae for electron scattering in Cox's opacity code causes no serious errors in the problem of neutron stars.

ENVELOPES AND THEIR CHARACTERISTICS

A computing program has been prepared for the 7094 computer which carries out the surface integrations and other related computations automatically. The program was constructed so that the equation of state automatically switched over from Equation (9) to (10) as soon as the point was reached where these two became equal. The surface boundary values were calculated through the subroutine for the atmosphere whenever a new set of values of radius R , mass M and photospheric temperature T_e of the star were given. The interval of integration $\Delta \ln P$ was automatically adjusted so that the change of every variable was kept smaller than a suitable preassigned limit. For a given $\ln T$ and $\ln \rho$ combination the corresponding opacity ($\ln \kappa$) was obtained by linear interpolation in the input opacity table. The surface boundary values of two typical models of stable neutron stars ($V_\beta, 0.6 M_\odot$) and ($V_\gamma, 2 M_\odot$) with a pure iron atmosphere are shown in Table 2.

To determine the temperature distribution in a typical neutron star envelope, the integration was first carried out from the photosphere down to the point where $\rho = 10^{14} \text{ gm/cm}^3$, for a representative model of $M = 1 M_\odot$ and $R = 10 \text{ km}$. This was repeated at several different surface temperatures. The results are shown in Table 3. The temperatures at different

densities are listed in terms of the given surface temperature T_e . T_b and ρ_b are the temperature and density where degeneracy starts (where equation (9) gives the same pressure as equation (10)). Degeneracy starts at about $\rho_b = 10^6 \text{ gm/cm}^3$ when $T_e \sim 10^7 \text{ }^\circ\text{K}$. But when the surface has cooled down to about $10^6 \text{ }^\circ\text{K}$, degeneracy sets in at $\rho_b = 10^4 \text{ gm/cm}^3$. A significant result is that even after the degeneracy boundary has been passed, the temperature still continues to go up as we go inwards. The fractional rise in temperature as the density increases from 10^6 to 10^9 gm/cm^3 is about 10% when $T_e = 7.7 \times 10^5 \text{ }^\circ\text{K}$, but at $T_e = 10^7 \text{ }^\circ\text{K}$ the temperature at the point $\rho = 10^9 \text{ gm/cm}^3$ is about 3 times that at $\rho = 10^6 \text{ gm/cm}^3$. As we go in toward the center from the point with $\rho = 10^9 \text{ gm/cm}^3$ to $\rho = 10^{12} \text{ gm/cm}^3$, the fractional rise in temperature is about 0.5% for $T_e = 10^6 \text{ }^\circ\text{K}$ and about 3% for $T_e = 10^7 \text{ }^\circ\text{K}$. The table shows that the temperature gradient is completely negligible for density higher than about 10^{12} gm/cm^3 . The conclusion is that the temperature gradient is very high in the outermost thin non-degenerate layers, the temperature continues to rise as we go through the degenerate outer layers of heavy ions and electrons, but the inner neutron core (with $\rho \gtrsim 10^{12} \text{ gm/cm}^3$) is isothermal even for the models of the hottest neutron stars. Hence, the core temperature T_c (which

is also the central temperature of the star) can be defined as that temperature where $\rho=10^{12}$ gm/cm³.

The central temperatures are plotted against surface temperatures in Figure 2. The solid curves are for Fe and the dashed curves are for Mg atmospheres. Curves drawn for three models of the V_v type are marked by the corresponding mass. Similar but simpler calculations were made by Chiu and Salpeter (1964) and Morton (1964). Their central temperature was defined to be the temperature where the degeneracy sets in (our T_b), but we have noted that the temperature continues to rise considerably as we go inwards passing the degeneracy boundary ($T_c > T_b$). Therefore, our central temperature should be higher than their values in general. However, in high temperature regions where the electron scattering is the most important mechanism for the opacity, they used the constant value $\kappa \sim 0.2$ cm²/gm, Thomson scattering opacity, while the Compton scattering included in Cox's code which we used lowers the opacity from the constant value of Thomson scattering. This, in effect, lowers our values of central temperature. These two causes of discrepancy compensate one another and there is good general agreement among our results and their results for $T_c > 10^9$ °K. We see in Figure 2 that the central temperature is somewhat lower for Mg than Fe at the

same surface temperature. This is due to the fact that somewhat lower opacities are associated with Mg than Fe as is revealed in Figure 1. For some of the coolest neutron stars ($T_e \sim 10^4$ °K) the central temperature is only about 10 times the surface temperature, while for hot models (of $T_e \sim 10^7$ °K) the core is about 100 times as hot as the surface. In any case, however, the ratio of the central temperature to the surface temperature is quite small as compared with that of ordinary stars.

To examine the region near the surface more in detail, temperature is plotted against distance from the photosphere as measured inward in Figure 3. Each curve is marked by the surface temperature. The model with one solar mass and 10 km radius is used to illustrate the general behavior of the surface properties. The crosses marked by $\chi=2.5$ represents points where the degeneracy starts. This criterion for degeneracy is derived from the fact that the kinetic energy of a non-relativistic fermion (about $3/5$ of the Fermi energy E_F) and the thermal energy of a free particle with no internal degrees of freedom ($3kT/2$) should be equal at the boundary between the non-degenerate and degenerate layers. The result of the present calculations shows that even for the hottest models degeneracy starts before we go inward by 100

meters from the surface and that the non-degenerate layers are less than 1% in thickness for even the hottest models. The mass contained in the non-degenerate envelopes is practically zero. In our previous paper (Tsuruta and Cameron 1966) it is seen that the amount of mass contained even in the inner degenerate electron-ion envelopes is very small compared to the total stellar mass. These results more than justify our previous assumption of constant mass and radius in the atmospheric calculations and also the neglect of non-degenerate layers in determining the total mass and radius of the star in our previous paper (Tsuruta and Cameron 1966). Hot neutron stars with $T_e \sim 10^7$ °K have non-degenerate envelopes of about 10~20 meters thick but when the surface temperature falls to about a million degrees the thickness of the non-degenerate layers becomes only about a meter or so. A typical neutron star with the sun's mass, 10 km radius, and 6.7×10^6 °K at the surface (with $\sim 100 L_{\odot}$) is shown to have non-degenerate envelopes of 3~4 meters.

The density profile near the surface is plotted in Figure 4 for the same model. The distance from the surface is now shown in centimeters. Within about a meter (0.01% of the radius) from the photosphere, the density rises to about 10^5 gm/cm³ when $T_e \sim 10^6$ °K and to about $10^{2.5}$ gm/cm³ for

hotter stars ($T_e = 1.6 \times 10^7$ °K). In the photosphere the density rises within a thickness of 10 cm by a factor of about 100 for typical models ($T_e \sim 10^6$ °K). In any case a sharp drop of density from the central value ($10^{14} \sim 10^{15}$ gm/cm³) to the photospheric value (0.01~1 gm/cm³) occurs only at the very edge of the star.

The distribution of density, temperature and degree of degeneracy E_F/kT within the thin layers about 10 meters from the surface are numerically shown in Table 4 at several interesting values of surface temperature. On comparing this table with the previous one, we see that the degeneracy criterion used in these two tables agrees well with each other.

The conclusion according to the present calculation is that neutron stars of about 10^3 times solar luminosity are as hot as 10^7 °K at the surface and about $10^{9 \sim 10}$ °K in the interior, those which are as luminous as the sun (in the x-ray region) are about $1 \sim 2 \times 10^6$ °K at the surface and about $10^{8 \sim 9}$ °K in the interior, and that by the time they cool down to the point where $T_c \sim 10^{6 \sim 7}$ °K and $T_e \sim 10^5$ °K they are too faint to be detected ($L \sim 10^{-5} L_\odot$). In our previous papers (Tsuruta and Cameron 1965b, 1966) it was shown that the composition of the surface layers changes sharply from layer to

layer. Starting from the boundary between the neutron core and the degenerate electron-ion envelopes the composition changes from more neutron-rich heavy nuclei to less neutron-rich ones as we go outwards. In the outermost non-degenerate layers with $\rho < 10^6$ gm/cm³, the main equilibrium composition should be ordinary iron group nuclei. This is why iron was chosen in our opacity calculations.

A possible change of surface composition can occur if a diffusion process is present. The diffusion process can become quite efficient in the presence of very small density scale heights and large gravity effects, as is the case in the atmospheres of neutron stars. Rough estimates of the effect of diffusion on the surface composition of neutron stars were made by Chiu and Salpeter (1964). Their conclusion is that some lighter elements such as Mg, O and Ne can be present on the surface of neutron stars. This is why not only Fe but also Mg was selected in our opacity and atmospheric calculations earlier. The change of composition will not occur if convective mass motions in non-degenerate layers cause efficient mixing of elements. In this case the original statistical equilibrium composition of iron will be maintained. However, convection appears to play no important role in neutron star problems since

the temperature gradients in our model atmospheres are all subadiabatic. At the present time, the effect of the diffusion is not known. However, the difference between our results for Fe and Mg compositions is relatively small. This indicates that the uncertainty of surface composition due to the effect of diffusion will not cause any serious errors in our results presented in this paper. We will see that the uncertainties due to other effects are far greater.

ENERGY CONTENT OF A NEUTRON STAR

If we assume that a neutron star belongs to the end state of a thermonuclear evolution, there can be no energy generation within it. Any stable neutron star is already so dense that gravitational potential energy due to contraction is not available. Even though the matter is highly degenerate, the only contribution to the total energy of a stationary neutron star comes from the small tail of the Fermi distribution function of the particles which constitute the star. The heat capacity of a nearly zero-temperature ideal Fermi gas was derived by Chandrasekhar (1957). Using his result, the total thermal energy of a neutron star was found to be

$$(16) \quad U = \left[\int_0^R \sum_i \left(\frac{\pi^2 k^2}{m_i c^2} \frac{(\chi_i^2 + 1)^{1/2}}{\chi_i^2} \right) n_i 4\pi r^2 dr \right] \frac{T^2}{2}$$

where $\chi_i = P_i^F / (m_i c)$

m_i , P_i^F and n_i are the mass, Fermi momentum and number density of the i^{th} particle, R is the stellar radius and T is the temperature of the isothermal core. The summation was taken over all the baryons and leptons present in each layer dr . The total energy was calculated as a function of temperature for our models. The results are shown in Tables 5 - 10. It is seen that as the surface temperature of a star decreases from about 5×10^7 °K to 10^4 °K the energy content of the star decreases from about 10^{50} ergs to 10^{40} ergs, although the precise value depends on the type of model in question.

In the above derivation the nuclear interaction between particles was neglected. The presence of nuclear forces will modify the heat capacity by an amount which typically can be of the order of factor 2, according to rough estimates which we have made. We did not take such modifications into account in making the actual cooling calculations, because the uncertainties arising from other sources are far greater.

NEUTRINO LUMINOSITY

The conserved vectorcurrent theory of weak interactions predicts that neutrino-antineutrino pairs can be radiated in quantum electrodynamic processes as well as electromagnetic

radiation. Even though the probability for the neutrino radiation is enormously small, it plays an extremely important role in some stages of stellar evolution because of the fact that the neutrino mean free path is so large that it can escape even from a dense star with hardly any interaction, while electromagnetic radiation can only diffuse out very slowly from the interior to the surface. Various different neutrino processes possible in a stellar interior have been examined. Consequently, the following three processes have been found to be the most important in the problem of neutron stars.

(1) Neutrino pair emission from the plasma process:

$$(17) \quad \nu(\text{plasmon}) \rightarrow \nu_e + \bar{\nu}_e$$

These neutrinos arise from the decay of plasmons in the degenerate electron gas in the interior of the neutron star. The rates are given by (Adams, Ruderman and Woo 1963, Inman and Ruderman 1964):

$$Q_{p1} \text{ (ergs/cm}^3\text{-sec)} = 1.228 \times 10^{22} \left(\frac{\hbar \omega_0}{m_e c} \right)^9 F(\chi)$$

where

$$F(\chi) = \sum_{n=1}^{\infty} \frac{K_2(n\chi)}{n\chi} \quad \text{or}$$

$$\chi^3 F(\chi) = 2\zeta(3) + \frac{1}{2}\chi^2 \ln \chi - \frac{1}{4}(2\ln 2 + 1)\chi^2 + \chi^4 \frac{\ln \chi}{96}$$

$$-\frac{1}{96} \left(\ln 2 - \frac{1}{4} + \ln 2\pi - \frac{\zeta'(2)}{\zeta(2)} \right) \chi^4 \quad \text{for } \chi < 2\pi$$

(18)

$$\zeta(3) = \sum_{n=1}^{\infty} \left(\frac{1}{n^3} \right); \zeta(2) = \sum_{n=1}^{\infty} \left(\frac{1}{n^2} \right) = \frac{\pi^2}{6}; -\zeta'(2) = \sum_{n=1}^{\infty} \frac{\ln n}{n^2}$$

$$\chi = \frac{\hbar \omega_0}{kT}, \quad \omega_0^2 = 4\pi e^2 \int d^3P \frac{f(\bar{P})}{E_P} \left(1 - \frac{1}{3} \frac{\bar{P}^2}{E_P^2} \right) \approx 4e^2 P_F^3 / (3\pi E_F)$$

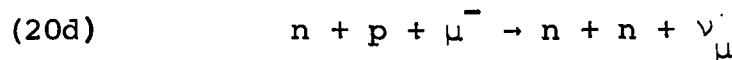
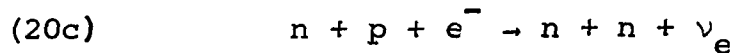
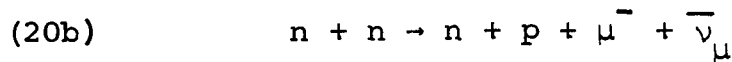
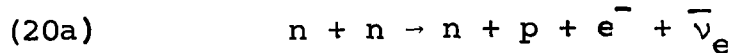
$$E_F = (P_F^2 + m_e^2)^{1/2}, \quad P_F = (3\pi^2 n_e)^{1/3}$$

for relativistic degenerate electrons. (In the last three equations the units are $\hbar = c = 1$.) Then the neutrino luminosity due to the plasma process is

$$(19) \quad L_{\nu}^{pl} = \int_0^R Q_{pl} 4\pi r^2 dr \text{ (ergs/sec)}$$

To evaluate the above integral, a table listing $F(\chi)$ as a function of χ and the interpolation subroutine were used. The plasma neutrino emission rates have been calculated as a function of temperature and electron number density and are shown in Figure 5.

(2) The URCA process (the beta process and its inverse process): In the interior of a neutron star it can be represented by reactions such as:



The approximate formulas for the rates of these processes

for a neutron star of uniform density distribution have been derived by Bahcall and Wolf (1965c). We applied their results to our neutron star models. The neutrino luminosity due to the URCA process can then be given by

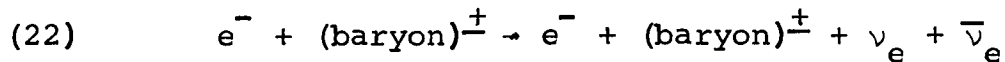
$$L_{\nu}^{\text{URCA}} = \int_0^R 10^{20} (1+F) T_9^8 (\rho/\rho_{\text{nucl}})^{2/3} 4\pi r^2 dr \text{ (ergs/sec)}$$

$$(21) \quad F = P_F(\mu) / P_F(e) = [1 - 2.25 (\rho_{\text{nucl}}/\rho)^{4/3}]^{1/2} \text{ for } \rho > 1.8 \rho_{\text{nucl}}$$

$$= 0 \text{ for } \rho < 1.8 \rho_{\text{nucl}}$$

where ρ is the density of the neutron star matter, ρ_{nucl} is the density of nuclear matter ($= 3.7 \times 10^{14} \text{ gm/cm}^3$), T_9 is the stellar temperature in units of 10^9 K , $P_F(i)$ is the Fermi momentum of the i^{th} species.

(3) The neutrino bremsstrahlung process: In the interior of a neutron star it can be symbolically expressed as



The neutrino pairs are emitted when electrons scatter from positive or negative baryons in the interior of the neutron star. Ruderman and Festa (private communication) have kindly provided us with the following approximate preliminary expression for this process:

$$(23) \quad Q_B \text{ (ergs/gm-sec)} = 10^6 Z^2 \frac{n_Z}{n} (T_9)^6 \text{ for } E_F \gg mc^2$$

where Z is the effective charge of the electron scattering centers, n_Z is the number density of such centers, and n we take here to be the baryon number density. Ruderman and Festa have suggested that there may be proton clustering in neutron star interiors in the presence of very large numbers of neutrons, so that the effective charge of a scattering center might be 2. However, for some of the massive neutron stars in which the density exceeds about 10^{15} gm/cm³ there will also be a large number of Σ^- hyperons, which may hinder the clustering process. In such a case, we have chosen to take the effective charge of a scattering center to be 1 and to count as the scattering centers both the protons and the Σ^- hyperons. The possible error caused by the uncertainty due to the different interpretation of the scattering centers and the effective charge is in any case negligible in our present problem. The neutrino luminosity due to the bremsstrahlung process is

$$(24) \quad L_V^B = \int_0^R Q_B \rho 4\pi r^2 dr \text{ (ergs/sec) .}$$

The total luminosity is obtained by adding all the contributions

$$(25) \quad L = L_{\text{ph}} + L_{\nu}^{\text{Pl}} + L_{\nu}^{\text{URCA}} + L_{\nu}^{\text{B}} .$$

L_{ph} is the photon luminosity defined by (12).

The results are shown in Tables 5-10. To visualize the contributions of different processes, the three different neutrino luminosities and photon luminosity, together with the total energy, are plotted against the central temperature for the model $(V_{\gamma}, 1.1M_{\odot})$ and shown in Figure 6. At higher temperatures the URCA process and the plasma neutrino process compete with each other but the URCA process is always the most important. At lower temperatures the URCA process competes with the bremsstrahlung process but the plasma process becomes unimportant. At sufficiently low temperatures the bremsstrahlung process predominates over other neutrino processes. The point where the bremsstrahlung rate begins to exceed the URCA rates depends on the stellar mass. For massive stars, this switching occurs at $3 \sim 8 \times 10^9 \text{ }^{\circ}\text{K}$, but for low mass stars the switching temperature is $\sim 5 \times 10^7 \text{ }^{\circ}\text{K}$. Neutrino cooling of any kind becomes too small as compared with the photon cooling when the temperature becomes lower than about $1 \sim 4 \times 10^8 \text{ }^{\circ}\text{K}$. Hence, the bremsstrahlung process never becomes important in sufficiently low mass stars ($M \sim 0.2M_{\odot}$).

In the above luminosity calculations we assumed that all neutrino processes not included here are unimportant in neutron stars. Bahcall and Wolf (1965a,c) have raised the question of neutrino cooling from pion decays in neutron star interiors. Such pion decays can occur only if pions should have a small effective mass in the presence of a largely neutron gas. Both Bahcall and Ruderman, as well as others, have indicated to us (private communication) their expectation that, under the conditions in which pions may be present in a neutron star, there will be a predominantly repulsive interaction between the pions and the neutrons. This would raise, rather than lower, the effective mass of the pions, and make it very unlikely that pions will be present in the interiors of neutron stars.

COOLING TIMES

The cooling time τ is computed from the various theoretical data of the last sections and from the following relation:

$$(26) \quad \tau = - \int_{U_1}^{U_2} \frac{dU}{L(U)}$$

where U is the total energy content of a star and $L(U)$ is the total luminosity, $L_{\text{ph}} + \Sigma L_{\nu}$, expressed as a function of U . If the above integration is carried out from the initial energy U_1 to the final energy U_2 , τ gives the time interval during which the star has cooled from a higher temperature T_1 where the total energy is U_1 to a lower temperature T_2 where the total energy is U_2 . The moment at which a supernova explodes has been defined as the starting point for counting the age of a neutron star.

The results are tabulated in Tables 5 through 10. An important parameter which characterizes the cooling behaviour is the ratio of the central temperature to the surface temperature, a typical value of which is about 100 for a neutron star. Hence we defined α as the ratio of the central temperature to the surface temperature in units of 100, and the values of α for each model at different temperatures are listed in the same tables. We see that this ratio is a sensitive function of mass, temperature, composition and nuclear potential. With increase in mass, α decreases. With increase in temperature, α increases. For the models of the same mass, temperature and nuclear potential, the value of α for Fe models is somewhat larger than that for Mg models.

We see that the detailed behavior of cooling is different for each different type of model and that this difference comes mainly through the sensitive dependence of α on the different kind of model.

Figure 7 shows the cooling curves of our six models with iron atmospheres (solid curves correspond to V_{β} type and dashed curves to V_{γ} type models). The point at which the neutrino cooling rate and the photon cooling rate become equal is shown by a cross for each curve. The figure shows that for the same nuclear potential, the neutron stars of lower mass cool faster than those of larger mass up to an age of about 10^6 years, but after that the heavier neutron stars cool somewhat faster.

The complicated effect of the nuclear potential is observed when we compare the curves of the models of the same temperature and mass but of different nuclear potential. To see better the effects of different composition, cooling curves for the same types of model of the same masses but of different compositions are shown in Figure 8. Solid curves represent models with iron atmospheres and dashed curves those with Mg atmospheres. We see that in the region where the neutrino cooling predominates over the photon cooling

the cooling rates of Fe models are somewhat faster than the cooling rates of Mg models, but that the reverse situation is noted in the region where the photon cooling is the main cooling mechanism. This is easily explained if we note that the neutrino cooling and the total energy content of the star depend on the internal temperature while the photon cooling is a function of the surface temperature and that the opacity of Mg atmospheres is somewhat lower than the opacity of Fe atmospheres.

We see in these figures that the models with $T_e \gtrsim 10^7$ °K cool too fast for observation, while the strong absorption of x-rays from a neutron star by interstellar gases makes it very difficult for us to observe neutron stars with $T_e < 10^6$ °K. The star's luminosity itself is already low at $T_e \sim 10^6$ °K (Table 2). Hence the most important range of temperature of neutron stars from the point of view of observation is $10^7 > T_e > 10^6$ °K, and this portion of the curves is enlarged in Figure 9. A neutron star will be only about 1 day to 10 years old when $T_e \sim 10^7$ °K depending on its mass value, nuclear potential and surface composition, but it will take about 2×10^3 to 3×10^5 years before it will cool down to $\sim 10^6$ °K. We note that the effect of mass on cooling time is

the most drastic. The dependence of cooling on the different possible kinds of nuclear potential and composition is by no means negligible when we need detailed theoretical information, but this uncertainty is relatively small as compared with the mass effect. By comparing our present results with the original calculations (Tsuruta 1964) where only the plasma process was taken into account as the neutrino cooling mechanism, we note that the faster rates of cooling by the URCA process and the bremsstrahlung process cause some important effects on the cooling behavior at higher temperatures ($T_e \gtrsim 2 \times 10^6$ °K), but no significant change is observed when $T_e < 2 \times 10^6$ °K.

OBSERVATIONAL PROBLEMS

If a neutron star emits radiation as a black body, the wavelength λ_{\max} giving the maximum intensity in the spectrum is given by

$$(27) \quad \lambda_{\max}(\text{cm}) = hc / (4.9651kT_e) = 0.2918 / T_e (\text{°K}) .$$

This simple relation indicates that when $T_e \sim 10^6$ to 10^7 °K the maximum comes in the soft x-ray region, $30 \gtrsim \lambda_{\max} \gtrsim 3\text{Å}$, while this maximum shifts to the ultraviolet region when T_e

falls to around $10^5 - 10^4$ °K. From Table 2 we see that a neutron star with $T_e > 10^6$ °K has $L > L_{\odot}$ (L_{\odot} is the luminosity of the sun), while $L \sim 10^{-5} L_{\odot}$ to $10^{-9} L_{\odot}$ when $T_e \sim 10^5$ to 10^4 °K. Also it takes about 10^3 to 4×10^5 years before a neutron star cools down to $T_e \sim 10^6$ °K. That is, a neutron star can last sufficiently long to allow our observation in the x-ray regions even though it will be too faint to be seen optically.

Until recently the observation of x-rays from outer space has been prevented due to the fact that the earth's atmosphere is strongly opaque to radiation in the x-ray regions. However, interstellar gases are practically transparent to x-rays of, say, $\lambda \lesssim 30\text{\AA}$ (the precise value of the upper limit to the wavelength depends on the distance between us and the x-ray emitter). The above considerations lead us to the conclusion that some of the neutron stars which are sufficiently close to us and which are not surrounded by x-ray emitting gas clouds should be observable as x-ray sources.

Since it became possible to send x-ray detectors above the earth's atmosphere, at least 10 galactic x-ray sources have been discovered (Bowyer, Byram, Chubb and Friedman 1964a,

1964b, 1965, Giacconi, Gursky, Paolini and Rossi 1962, 1963, Fisher and Meyerott 1964). Two major sources which were discovered first which are best known are Sco XR 1, the strongest x-ray source in the constellation Scorpio, and Tau XR 1, a somewhat weaker source near the center of the Crab Nebula. We use the notation of Bowyer, Byram, Chubb and Friedman (1965) to designate x-ray sources. A possible association of the strongest Scorpius source and the North Polar Spur, the nebular remains of a supernova explosion which was supposed to have occurred about 50,000 to 100,000 years ago at a distance of about 30 parsecs away (Brown, Davies and Hazzard 1960), has been suggested, but otherwise there is no nebulosity or peculiar star in the vicinity of Sco XR 1. The Crab Nebula is believed to be the remnant of a supernova explosion which occurred in 1054 AD about 1100 parsecs away from us. The angular size of the Sco XR 1 was determined to be less than 7 minutes of arc (Oda, Clark, Garmire, Wada, Giacconi, Gursky and Waters 1965), while the size of the x-ray source in the Crab Nebula was measured to be about 1 light year in diameter through the lunar occultation experiment (Bowyer, Byram, Chubb and Friedman 1964b), less than half the size of the optical nebula in the Crab,

while the optical nebula is about two to three times smaller than the radio size. The flux of Sco XR 1 is about 10^{-7} ergs/cm²-sec and that of the Tau XR 1 is about 10^{-8} ergs/cm²-sec. The intensity of other sources is about the same as that of the source in the Crab Nebula.

All of the x-ray sources, except the Scorpius source, lie close to the galactic plane and within 90° of the galactic center. This distribution resembles that of galactic novae. From this and other evidence it has been suggested that the probable origins of the x-ray sources are supernova outbursts (Bowyer, Byram, Chubb and Friedman 1965, Burbidge, Gould and Tucker 1965, Cameron 1965b,c, Morrison and Sartori 1965, Oda 1965, Hayakawa and Matsuoka 1964, Finzi 1965). Indeed there is no evidence against this assumption. Many important supernovas have not been identified with x-ray sources of strength comparable with that of the Scorpius source or the source in the Crab Nebula. This is easily explained if we note that these supernovas are far more distant from us than the Crab Nebula or the North Polar Spur. Most of the discovered x-ray sources are not identified with known radio or optical objects. This is also no contradiction to the supernova hypothesis if we note the possibility that some of the x-ray production mech-

anisms will have much longer lifetime than that of the optical or radio emissions.

As mentioned already, we believe that a remnant of a supernova explosion consists of a central condensed core in the form of a neutron star and of surrounding hot gas clouds in the form of expanding envelopes. How can we observe this complex assembly of matter? As far as the central core of neutrons is concerned there will be no hope of observation except as the emitter of soft x-rays in the narrow range of about 30 to 3\AA , because a hotter neutron star of $T_e > 10^7$ °K (corresponding to x-rays of $< 3\text{\AA}$) will cool too fast (within less than a day to 10 years) and a cooler neutron star of $T_e < 10^6$ °K (corresponding to x-rays of $> 30\text{\AA}$) will be too faint to be detected due to the strong interstellar absorption and the faintness of the star itself. The situation is more complicated in the expanding envelopes.

Due to the complex nature of a supernova remnant, the observed x-rays can be due to non-thermal radiation from the hot gas clouds, the thermal radiation from the neutron star, or a mixture of both. The question of whether the thermal component can be singled out from the non-thermal component in the case both are present can be determined if the relative

strength of each component is known. In order to make some sensible predictions of the possible nature of some of the x-ray sources and their relation to neutron stars, we will discuss Sco XR 1 and Tau XR 1. The data on other sources are still too scarce for this purpose. If we know the distance d and the photon luminosity L of a neutron star, the flux F of the thermal component of x-rays reaching the region just above our atmosphere is found from

$$(28) \quad F = L / (4\pi d^2) .$$

If we accept the tentative association of the North Polar Spur and Sco XR 1, the distance and the age of the neutron star in Scorpius are known. Taking surface temperatures of 1 or 2×10^6 °K, consistent with the soft x-ray fluxes measured by Friedman's group, the photon luminosity of the star can also be predicted. The results for our six models are shown in Table 11. The age of the star τ has been taken from our results in the previous section (Figures 7-9). If both the North Polar Spur and the x-ray source in Scorpius are indeed the remnants of a supernova explosion about 30 parsecs away and about $10^{4\sim 5}$ years ago, the low mass models of $M \lesssim 0.3M_{\odot}$ should be excluded because they are too young. However, some

massive models are sufficiently old to support this hypothesis. The flux of x-rays from a massive neutron star is also comparable with the observed x-ray flux from the Scorpius source. The result shown in Table 11 gives rise to a possibility that the observed x-rays from the Scorpius source may have a predictable amount of thermal component, if it contains a massive neutron star of about $1 \sim 2M_{\odot}$. The spectral measurements of Sco XR 1 were reported to be inconsistent with the picture of pure black-body radiation. This may suggest that the nonthermal component from the surrounding hot gas dominates over the thermal component from the neutron star sufficiently to obscure the black-body spectrum. However, because of the relatively strong flux from the neutron star as calculated above, the thermal component in this source may be identified, if the remnant star is massive enough, and if longer wavelength detectors can be used which are more sensitive to the peak of the thermal spectrum.

Next, consider the source in the Crab Nebula. Here, $\tau = 910$ years and we get the present temperature and luminosity from the results in the previous sections. The distance is about 1100 parsecs. From this information, the thermal component of the x-ray flux from a neutron star in the Crab Nebula can be obtained. The results are shown in Table 12,

for various models of different mass, nuclear potential and surface composition. We see that, with the exception of the particular model of V_γ type, Mg composition and about 2 solar masses, the flux is less than about 1/4 of the observed x-ray flux from Tau XR 1. The large size of about one light year already indicated that the major source of the x-rays from the Crab Nebula is not thermal emission from a neutron star. The theoretical calculation also supports this view. If a neutron star exists in the x-ray source, it will not be identified if the flux from the neutron star is too weak, as compared with that from the surrounding region.

We are indebted to Mr. B. Sackaroff for assistance with the opacity calculations which involved the use of some parts of the Los Alamos opacity code in regions of temperature and density for which the entire code does not work.

REFERENCES

- Adams, J.B., Ruderman, M.A., and Woo, C.H. 1963. Phys. Rev.,
129, 1383.
- Arnett, W.D. 1966. Thesis, Yale University.
- Bahcall, J.N. and Wolf, R.A. 1965a. Phys. Rev. Lett., 14, 343.
- _____ 1965b. Phys. Rev., 140, B1445.
- _____ 1965c. Phys. Rev., 140, B1452.
- Bowyer, S., Byram, E.T., Chubb, T.A., and Friedman, H. 1964a.
Nature, 201, 1307.
- _____ 1964b. Science, 146, 912.
- _____ 1965. Science, 147, 394.
- Brown, R.H., Davies, R.D., and Hazzard, C. 1960. Observatory,
80, 191.
- Burbidge, G.R., Gould, R.J., and Tucker, W.H. 1965. Phys. Rev.
Lett., 14, 289.
- Cameron, A.G.W. 1959a. Astrophys. J., 129, 676.
- _____ 1959b. Astrophys. J., 130, 884.
- _____ 1965a. Lecture notes at Yale University.
- _____ 1965b. Nature, 205, 787.
- _____ 1965c. Nature, 206, 1342.
- Chandrasekhar, S. 1957. An introduction to the study of stellar
structure (Dover, New York).
- Chodil, G., Jopson, R.C., Mark, H., Seward, F.D., and Swift, C.D. 1965.

- Phys. Rev. Lett., 15, 605.
- Chiu, H.Y. 1964. Annals of Phys., 26, 364.
- Chiu, H.Y. and Salpeter, E.E. 1964. Phys. Rev. Lett., 12, 413.
- Clark, G.W. 1965. Phys. Rev. Lett., 14, 91.
- Colgate, S.A. and White, R.H. 1965. to be published.
- Cox, A.N. 1961. preprint.
- Finzi, A. 1965a. Phys. Rev., 137, B472.
- _____ 1965b. Phys. Rev. Lett., 15, 599.
- Fisher, P.C. and Meyerott, A.J. 1964. Astrophys. J., 139, 123.
- Giacconi, R., Gursky, H., Paolini, F.R., and Rossi, B.B. 1962.
- Phys. Rev. Lett., 9, 439.
- _____ 1963. Phys. Rev. Lett., 11, 530.
- Giacconi, R., Gursky, H., and Waters, J.R. 1965. Nature, 207, 572.
- Hayakawa, S. and Matsuoka, M. 1964. Prog. Theor. Phys.,
- Suppl. 30, 204.
- Inman, C.L. and Ruderman, M.A. 1964. Astrophys. J., 140, 1025.
- Morrison, P. and Sartori, L. 1965. Phys. Rev. Lett., 14, 771.
- Morton, D.C. 1964. Nature, 201, 1308.
- Oda, M. 1965. Presented at the Cosmic Ray Conference of IUPAP,
London.
- Oda, M., Clark, G., Garmire, G., Wada, M., Giacconi, R., Gursky, H.,
and Waters, J. 1965. Nature, 205, 554.
- Sampson, D.H. 1959. Astrophys. J., 129, 734.

Schatzman, E. 1958. White Dwarfs (North-Holland Publishing Co., Amsterdam).

Schwarzschild, M. 1958. Structure and evolution of the stars (Princeton University Press, Princeton).

Tsuruta, S. 1964. Thesis, Columbia University (unpublished).

Tsuruta, S. and Cameron, A.G.W. 1965a. Nature, 207, 364.

_____ 1965b. Can. J. Phys., 43, 2056.

Tsuruta, S. and Cameron, A.G.W. 1966. to be published.

Zwicky, F. 1938. Astrophys. J., 88, 522.

_____ 1939. Phys. Rev., 55, 726.

_____ 1958. Handbuch der Physik (Springer-Verlag, Berlin).

51, 776.
M

TABLE CAPTIONS

Table 1: Characteristics of our six chosen models. The models are identified by the type of nuclear interaction V_β or V_γ and their approximate mass in solar mass units. ρ_m^c is the central density in cgs units, M/M_\odot is the mass in solar mass units, R is the stellar radius in km, and PC is the central pressure in relativistic units $\left(PC = \frac{P(\text{dynes/cm}^2)}{6.46 \times 10^{36}} \right)$.

Table 2: Photospheric properties of typical neutron stars ($V_\beta, 0.6M_\odot$) and ($V_\gamma, 2M_\odot$) at different surface temperatures T_e . L_{ph} is the photon luminosity, ρ_{ph} , P_{ph} and κ_{ph} are the photospheric density, pressure and opacity, respectively, and λ_{max}^o is the maximum wavelength without red shift correction.

Table 3: Atmospheric temperature distribution of neutron star models with $M = 1M_\odot$ and $R = 10$ km. The temperature T at a specified ρ , and the temperature T_b and density ρ_b where the degeneracy starts are listed as a function of surface temperature T_e .

Table 4: (Models with $M = 1M_\odot$, $R = 10$ km) Temperature and density distribution near the surface at different depths $(R-r)$ at given surface temperature T_e . The point where $E_F/kT = 2.5$ indicates the thickness of the non-degenerate envelopes.

Table 5: The characteristics of the hot neutron star model ($V_\gamma, 2M_\odot$) with the Fe and Mg atmospheres. (T_e and T_c are the surface and core temperatures, L_{ph} is the photon luminosity, ΣL_ν is the total neutrino luminosity, $\alpha = \left(\frac{T_c}{T_e} \right) 10^{-2}$, U is the internal energy and τ is the cooling time.)

Table 6: The characteristics of the hot neutron star model ($V_\gamma, 1.1M_\odot$) with the Fe and Mg atmospheres. (The notation is that used in Table 5.)

Table 7: The characteristics of the hot neutron star model ($V_\gamma, 0.2M_\odot$) with the Fe and Mg atmospheres. (The notation is that used in Table 5.)

Table 8: The characteristics of the hot neutron star model ($V_\beta, 1.0M_\odot$) with Fe atmospheres. (The notation is that used in Table 5.)

Table 9: The characteristics of the hot neutron star model ($V_\beta, 0.6M_\odot$) with Fe atmospheres. (The notation is that used in Table 5.)

Table 10: The characteristics of the hot neutron star model ($V_\beta, 0.2M_\odot$) with Fe atmospheres. (The notation is that used in Table 5.)

Table 11: The observational problem of Sco XR1. (T_e is the surface temperature, L_{ph} is the photon luminosity, τ is the age of the neutron star of the given temperature and FLUX is the flux of the thermal component of the x-rays from a neutron star in Sco XR1, 30 parsecs away, to be observed above the earth's atmosphere.)

Table 12: The observational problem of Tau XR1. (T_e is the surface temperature of the neutron star of age 910 years, L_{ph} is the photon luminosity of the neutron star of the given temperature, and FLUX is the flux of the thermal component of x-rays from the neutron star.)

TABLE 1

Model (Notation)	ρ_m^c (gm/cm ³)	M/M _⊙	R (km)	PC
V _γ , 0.2M _⊙	2.33x10 ¹⁴	0.2003	17.78	5x10 ⁻⁴
V _γ , 1.1M _⊙	6.89x10 ¹⁴	1.074	12.33	0.01
V _γ , 2M _⊙	2.17x10 ¹⁵	1.953	9.939	0.2
V _β , 0.2M _⊙	3.26x10 ¹⁴	0.1996	18.21	7x10 ⁻⁴
V _β , 0.6M _⊙	3.55x10 ¹⁵	0.5927	7.159	0.06
V _β , 1M _⊙	8.26x10 ¹⁵	0.9663	5.184	0.7

TABLE 3

SURFACE TEMPERATURE T_e ($^{\circ}\text{K}$)	INTERNAL TEMPERATURE T ($^{\circ}\text{K}$)				T_b ($^{\circ}\text{K}$)	ρ_b (gm/cm^3)
	$\rho=10^6 \text{ gm}/\text{cm}^3$	$\rho=10^9 \text{ gm}/\text{cm}^3$	$\rho=10^{12} \text{ gm}/\text{cm}^3$	$\rho=10^{14} \text{ gm}/\text{cm}^3$		
1.6×10^7	9.08×10^8	3.47×10^9	3.65×10^9	3.65×10^9	1.4×10^9	4.3×10^6
1.2×10^7	6.86×10^8	2.34×10^9	2.425×10^9	2.425×10^9	7.7×10^8	1.5×10^6
1×10^7	5.92×10^8	1.825×10^9	1.88×10^9	1.88×10^9	5.92×10^8	1×10^6
9.4×10^6	5.75×10^8	1.68×10^9	1.73×10^9	1.73×10^9	4.8×10^8	5.4×10^5
6.7×10^6	4.51×10^8	1.10×10^9	1.125×10^9	1.125×10^9	2.6×10^8	1.4×10^5
5.1×10^6	3.79×10^8	8.09×10^8	8.21×10^8	8.21×10^8	1.5×10^8	6.2×10^4
4.3×10^6	3.395×10^8	6.765×10^8	6.83×10^8	6.83×10^8	1.03×10^8	4.8×10^4
3×10^6	2.64×10^8	4.62×10^8	4.64×10^8	4.64×10^8	7.6×10^7	4×10^4
1×10^6	9.61×10^7	1.12×10^8	1.125×10^8	1.125×10^8	3.5×10^7	10^4
7.7×10^5	6.5×10^7	7.18×10^7	7.35×10^8	7.35×10^8	2.3×10^7	4.2×10^3

TABLE 4

(R-r) (meters)	$T_e = 7.7 \times 10^5$ OK			$T_e = 3 \times 10^6$ OK			$T_e = 6.7 \times 10^6$ OK			$T_e = 1.6 \times 10^7$ OK		
	$\log \rho$	$\log T$	E_F/kT	$\log \rho$	$\log T$	E_F/kT	$\log \rho$	$\log T$	E_F/kT	$\log \rho$	$\log T$	E_F/kT
0	-1.176	5.887	0.039	-1.095	6.477	0.0114	-0.854	6.826	0.0074	-0.605	7.204	0.0045
0.1	0.614	6.48	0.166									
0.2	2.317	7.002	0.63	1.55	7.23	0.118						
0.3	3.275	7.261	1.53									
0.4	3.888	7.432	2.765	2.637	7.565	0.284						
0.5	4.201	7.509	3.59				2.28	7.714	0.118	1.576	7.794	0.0332
0.6	4.430	7.561	4.61	3.337	7.734	0.564						
1	4.930	7.661	7.66	4.286	7.931	1.564	3.42	7.97	0.376	2.558	8.028	0.0865
2	5.49	7.73	15.7	5.315	8.210	3.935	4.628	8.284	1.165	3.567	8.339	0.203
3				5.69	8.32	5.43	5.317	8.463	2.215	4.166	8.505	0.348
4				5.92	8.40	6.38	5.710	8.576	3.14	4.638	8.623	0.539
5	5.89	7.80	24.3	6.09	8.45	7.42	5.939	8.638	3.865	5.004	8.709	0.770
6							6.106	8.680	4.52	5.312	8.783	1.054
7				6.23	8.50	8.32						
8							6.27	8.74	5.04	5.784	8.902	1.673
10	6.463	7.835	55	6.54	8.55	11.75	6.474	8.782	6.265	6.15	8.996	2.34

TABLE 5

T_e (°K)	Log L_{ph} (ergs/sec)	Log ΣL_ν (ergs/sec)		Log T_c (°K)		$\alpha = \left(\frac{T_c}{T_e}\right) 10^{-2}$		Log U (ergs)		Log τ (years)	
		Fe	Mg	Fe	Mg	Fe	Mg	Fe	Mg	Fe	Mg
5×10^7	39.6432	47.39		10.1265		2.67		50.26		-5.21	-4.34
2×10^7	38.0514	42.25	41.48	9.5177	9.4181	1.65	1.31	49.02	48.76	-1.43	-0.57
10^7	36.8474	39.39	38.19	9.1047	8.9791	1.27	0.955	48.19	47.87	1.09	1.66
5×10^6	35.6432	37.01	35.77	8.7666	8.5777	1.165	0.756	47.49	47.08	2.89	3.34
2×10^6	34.0515	34.01	33.34	8.2938	8.1520	0.986	0.710	46.51	46.25	4.50	4.55
10^6	32.8474	31.49	30.99	7.8299	7.7550	0.750	0.570	45.61	45.49	5.43	5.25
5×10^5	31.6432	28.63	28.01	7.3814	7.2794	0.480	0.3808	44.74	44.49	5.96	5.76
2×10^5	30.0515	24.71	34.34	6.7035	6.6704	0.253	0.2341	43.37	43.28	6.41	6.23
10^5	28.8474			6.2647	6.2157	0.184	0.1641	42.51	42.41	6.73	6.60
5×10^4	27.6433			5.7925	5.6951	0.124	0.0994	41.51	41.29	7.00	6.94
2×10^4	26.0515			5.1716	5.0180	0.0743	0.0521	40.29	40.01	7.61	7.29
10^4	24.8474			4.5990		0.0398					

TABLE 6

T_e (°K)	Log L_{ph} (ergs/sec)	Log ΣL_v (ergs/sec)		Log T_c (°K)		$\alpha = \left(\frac{T_c}{T_e}\right) 10^{-2}$		Log U (ergs)		Log τ (years)	
		Fe	Mg	Fe	Mg	Fe	Mg	Fe	Mg	Fe	Mg
5×10^7	39.8303	50.34		10.5407		6.945		50.88			
2×10^7	38.2385	44.41	43.65	9.7534	9.6952	2.836	2.480	49.31	49.21	-3.48	-2.91
10^7	37.0344	41.01	40.13	9.3347	9.2319	2.160	1.702	48.59	48.29	-0.74	0.18
5×10^6	35.8303	37.79	36.77	8.9533	8.8007	1.798	1.261	47.73	47.46	1.63	2.68
2×10^6	34.2386	34.75	33.31	8.5282	8.3253	1.686	1.059	46.84	46.47	4.08	4.63
10^6	33.0345	32.11	31.38	8.1178	8.0160	1.310	1.038	46.08	45.82	5.55	5.36
5×10^5	31.8304	29.01	28.37	7.6389	7.5400	0.871	0.693	45.09	44.89	6.08	5.89
2×10^5	30.2386	25.25	24.79	7.0080	6.9460	0.4408	0.4415	43.83	43.71	6.62	6.44
10^5	29.0345			6.5192	6.4775	0.3306	0.3000	42.84	42.75	6.96	6.77
5×10^4	27.8304			6.0681	6.0036	0.2340	0.2019	41.91	41.81	7.26	7.07
2×10^4	26.2387			5.4366	5.3218	0.1364	0.1050	40.69	40.49	7.59	7.43
10^4	25.0345			4.9261		0.0844		39.71		7.88	
6×10^3	24.1472			4.5167		0.0548		38.88		8.07	

TABLE 7

T_e (°K)	Log L_{ph} (ergs/sec)	Log ΣL_ν (ergs/sec)		Log T_c (°K)		$\alpha = \left(\frac{T_c}{T_e}\right) 10^{-2}$		Log U (ergs)		Log τ (years)	
		Fe	Mg	Fe	Mg	Fe	Mg	Fe	Mg	Fe	Mg
2×10^7	38.5563	48.78		10.2662		9.225		49.98		-5.8	
10^7	37.3552	44.51	44.01	9.7377	9.6770	5.458	4.750	48.91	48.77	-4.2	-3.35
5×10^6	36.1481	41.29	40.58	9.3197	9.2165	4.174	3.288	48.08	47.87	-1.19	-0.67
2×10^6	34.5564	37.38	36.01	8.8358	8.6595	3.424	2.281	47.12	46.76	1.68	2.60
10^6	33.3523	34.98	33.29	8.5162	8.3141	3.281	2.061	46.51	46.12	3.65	4.48
5×10^5	32.1481	31.74	30.79	8.1029	8.0004	2.536	2.000	45.74	45.51	5.59	5.61
2×10^5	30.5564	27.21	26.23	7.4816	7.3745	1.516	1.1828	44.44	44.25	6.72	6.23
10^5	29.3523	23.82	23.53	6.9866	6.9282	0.972	0.8495	43.41	43.26	7.11	6.76
5×10^4	28.1482			6.5045	6.4596	0.6398	0.576	42.51	42.37	7.41	7.19
2×10^4	26.5564			5.8944	5.8106	0.3921	0.3234	41.26	41.12	7.80	7.68
10^4	25.3523			5.4193		0.2621		40.33		8.08	
6×10^3	24.4649			5.0643		0.1937		39.61		8.28	

T A B L E 8

T_e (°K)	$\text{Log } L_{\text{ph}}$ (ergs/sec)	$\text{Log } \Sigma L_{\nu}$ (ergs/sec)	$\text{Log } T_c$ (°K)	$\alpha = \left(\frac{T_c}{T_e}\right) 10^{-2}$	$\text{Log } U$ (ergs)	$\text{Log } \tau$ (years)
5×10^7	39.0778	45.86	10.0189	2.039	45.48	-4.26
2×10^7	37.4861	41.25	9.4351	1.361	48.51	-1.10
10^7	36.2819	38.91	9.0348	1.083	47.51	0.615
5×10^6	35.0778	36.98	8.7037	1.011	46.84	2.10
2×10^6	33.4861	34.03	8.2153	0.821	45.34	4.08
10^6	32.2820	31.03	7.7379	0.546	44.88	5.16
5×10^5	31.0779	28.38	7.2934	0.393	44.01	5.78
2×10^5	29.4861		6.6211	0.209	42.71	6.25
10^5	28.2820		6.1785	0.156	41.78	6.54
5×10^4	27.0779		5.7030	0.101	40.86	6.81
2×10^4	25.4862		5.0704	0.0589	39.61	7.19

T A B L E 9

T_e ($^{\circ}$ K)	Log L_{ph} (ergs/sec)	Log $\dot{E}_{L \nu}$ (ergs/sec)	Log T_c ($^{\circ}$ K)	$\alpha = \left(\frac{T_c}{T_e} \right) 10^{-2}$	Log U (ergs)	Log τ (years)
5×10^7	39.3581	48.76	10.4016	6.35	50.24	-6.5
2×10^7	37.7663	43.15	9.6815	2.40	48.74	-2.49
10^7	36.5622	39.51	9.2635	1.831	47.88	0.03
5×10^6	35.3581	37.56	8.8957	1.571	47.17	1.73
2×10^6	33.7664	35.01	8.4669	1.463	46.30	3.54
10^6	32.5623	32.58	8.0372	1.089	45.51	4.93
5×10^5	31.3582	29.65	7.5651	0.736	44.60	5.86
2×10^5	29.7664	25.81	6.9072	0.4046	43.26	6.51
10^5	28.5623		6.4444	0.2783	42.30	6.85
5×10^4	27.3582		5.9847	0.193	41.35	7.14
2×10^4	25.7665		5.3599	0.1144	40.10	7.49
10^4	24.5624		4.8191	0.0659	39.03	7.74
6×10^3	23.6750		4.4320	0.0451	38.30	7.95

T A B L E 10

T_e (°K)	Log L_{ph} (ergs/sec)	Log ΣL_ν (ergs/sec)	Log T_c (°K)	$\alpha = \left(\frac{T_c}{T_e}\right) 10^{-2}$	Log U (ergs)	Log τ (years)
2×10^7	38.5772	48.73	10.2798	9.53	50.01	-6.99
10^7	37.3731	44.61	9.7459	5.56	48.91	-4.07
5×10^6	36.1690	41.30	9.3277	4.253	48.12	-1.39
2×10^6	34.5772	37.48	8.8417	3.472	47.12	1.30
10^6	33.3731	34.99	8.5226	3.331	46.50	3.38
5×10^5	32.1690	31.70	8.1107	2.579	45.68	5.36
2×10^5	30.5773	27.10	7.4900	1.546	44.40	6.70
10^5	29.3731	24.00	6.9971	0.975	43.44	7.09
5×10^4	28.1690		6.5122	0.650	42.50	7.39
2×10^4	26.5773		5.9057	0.4026	41.26	7.74
10^4	25.3732		5.4286	0.2681	40.51	8.01
6×10^3	24.4858		5.0769	0.199	39.60	8.20

TABLE 12

		$(V_Y, 0.2M_{\odot})$	$(V_Y, 1.1M_{\odot})$	$(V_Y, 2M_{\odot})$	$(V_{\beta}, 0.2M_{\odot})$	$(V_{\beta}, 0.6M_{\odot})$	$(V_{\beta}, 1M_{\odot})$
Log T_e ($^{\circ}K$)	Fe	6.11	6.500	6.660	6.05	6.4	6.51
	Mg	6.254	6.655	6.785			
L_{ph} (ergs/sec)	Fe	7.024×10^{33}	1.087×10^{35}	3.06×10^{35}	3.742×10^{33}	1.454×10^{34}	2.10×10^{34}
	Mg	2.334×10^{34}	4.101×10^{35}	9.69×10^{35}			
FLUX 2 (ergs/cm 2 -sec)	Fe	4.85×10^{-11}	7.499×10^{-10}	2.12×10^{-9}	2.583×10^{-11}	1.003×10^{-10}	1.449×10^{-10}
	Mg	1.609×10^{-10}	2.828×10^{-9}	6.7×10^{-9}			

FIGURE CAPTIONS

Figure 1: The opacity in cm^2/gm as a function of density in gm/cm^3 , at different temperatures, calculated by the use of Cox's opacity code and an ionization code. Solid curves are for iron and dashed curves are for magnesium.

Figure 2: Central temperature as a function of surface temperature for models of nuclear potential V_γ with different mass values. Solid curves are for iron and dashed curves are for magnesium.

Figure 3: Temperature distribution near the surface of a neutron star. The temperature is plotted against the distance from the photosphere in meters for a model of one solar mass, 10 km radius, and with various different values of the surface temperature T_e . The borders between the degenerate layers and non-degenerate layers are shown by crosses.

Figure 4: Density distribution near the surface of a neutron star. The density is plotted against the distance from the photosphere in cm for a model of one solar mass, 10 km, and with various different values of the surface temperature.

Figure 5: Energy loss rates due to neutrino pair emission from plasma in $\text{erg}/\text{cm}^3\text{-sec}$ shown as a function of electron number

density in cm^{-3} at different temperatures.

Figure 6: Neutrino and photon luminosities and total internal energy of a neutron star model of 1.1 solar mass and of the V_γ type nuclear potential are shown as functions of the core temperature of the star. The neutrino luminosity L_ν due to the plasma process, the URCA process and the bremsstrahlung process are shown separately. The photon luminosity for the Mg atmosphere and the Fe atmosphere are also shown separately.

Figure 7: Cooling curves for the six typical neutron star models with iron atmospheres. Surface temperatures are plotted as functions of time in years. Solid curves represent the models with the V_β type nuclear potential and the dashed curves represent the models with the V_γ type potential. Different models are identified by their mass values and the type of the potential. The points where the major cooling mechanism shifts from the neutrino emission to the photon emission are indicated by the crosses.

Figure 8: The effect of composition on cooling curves. Surface temperatures of models of the V_γ type potential and with different mass values are plotted as functions of time in years for iron atmospheres (solid curves) and magnesium

atmospheres (dashed curves).

Figure 9: Cooling curves for models with iron atmospheres in the most interesting region for observation are shown in detail.

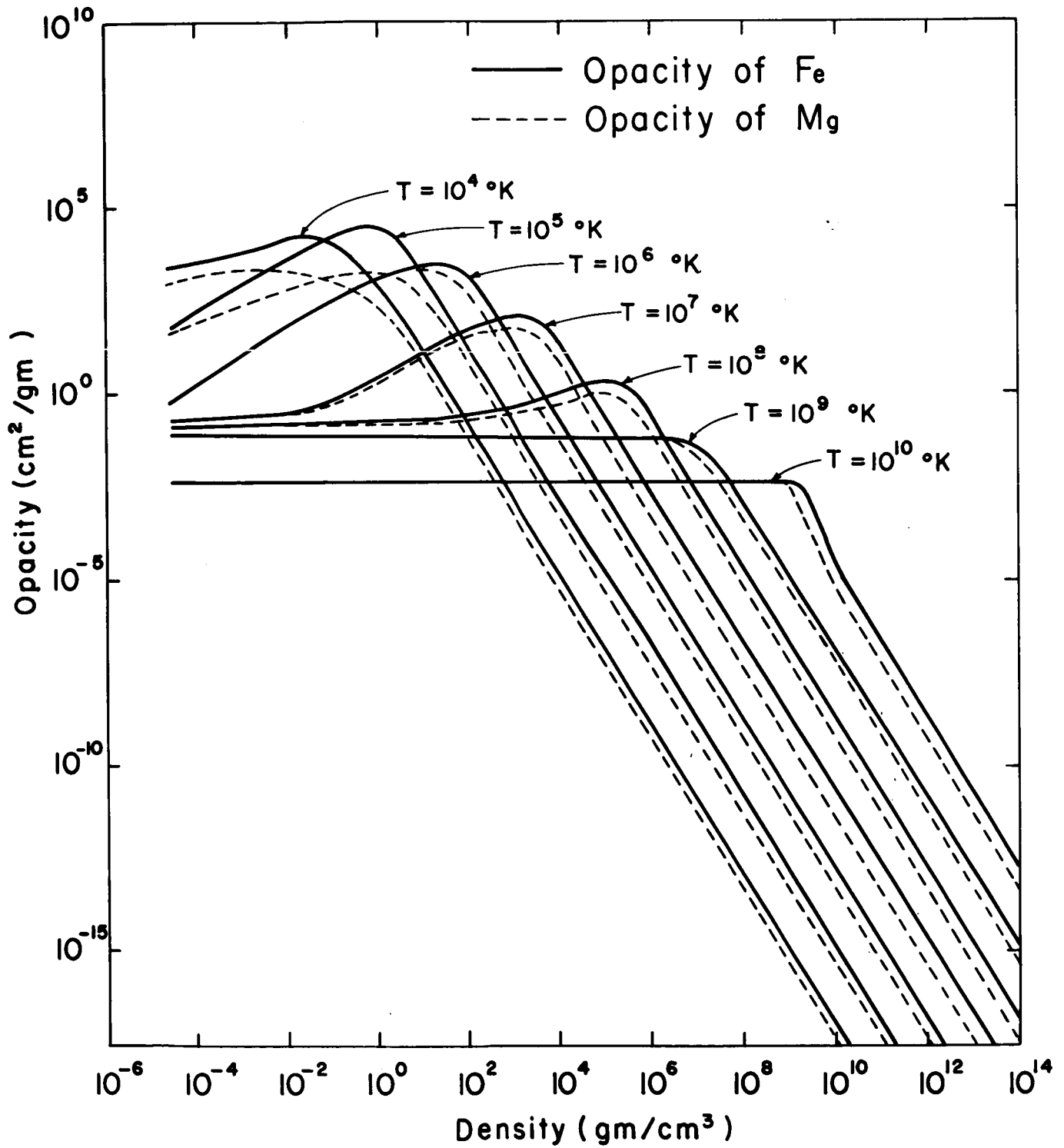


Figure 1

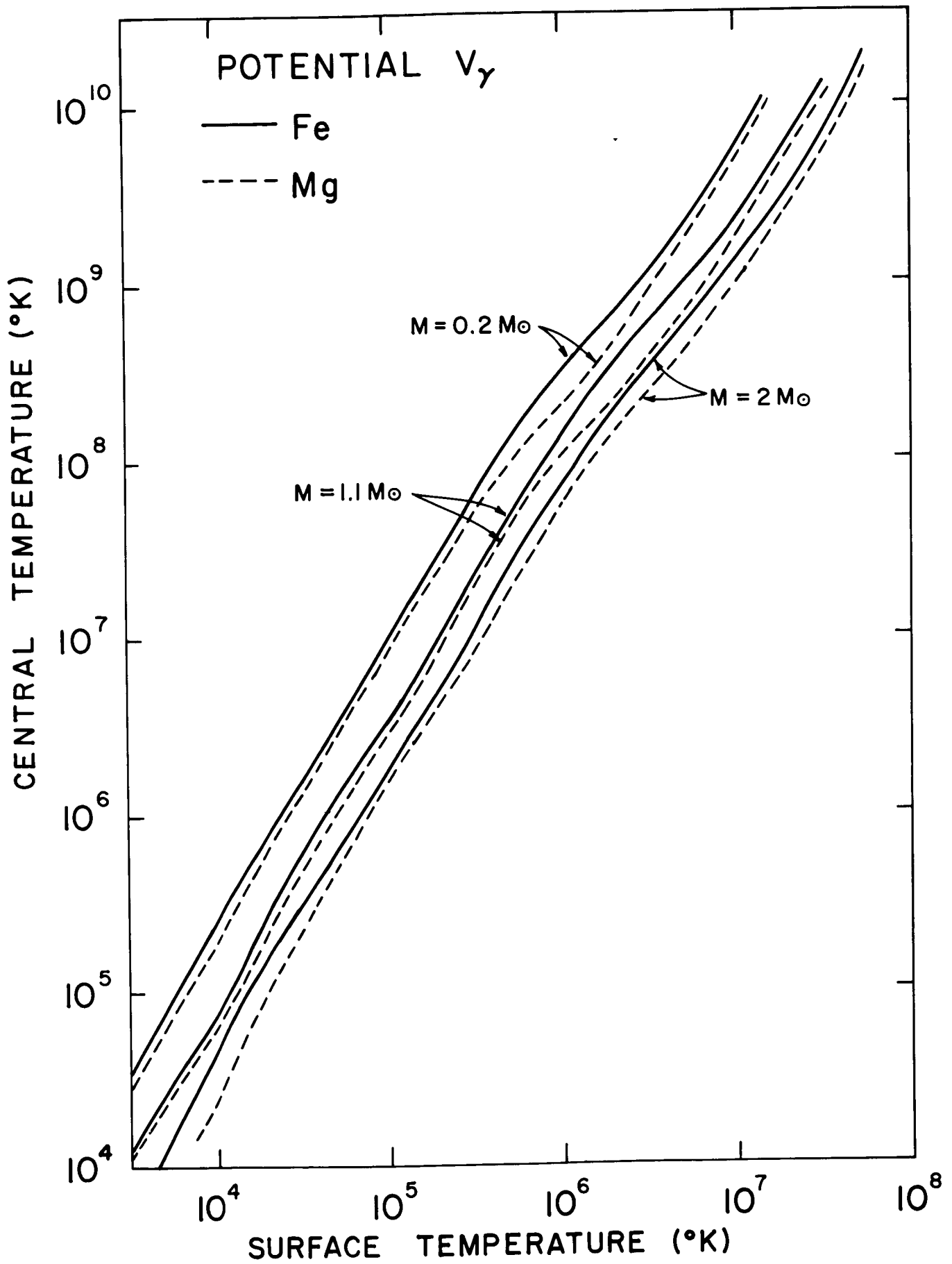


Figure 2

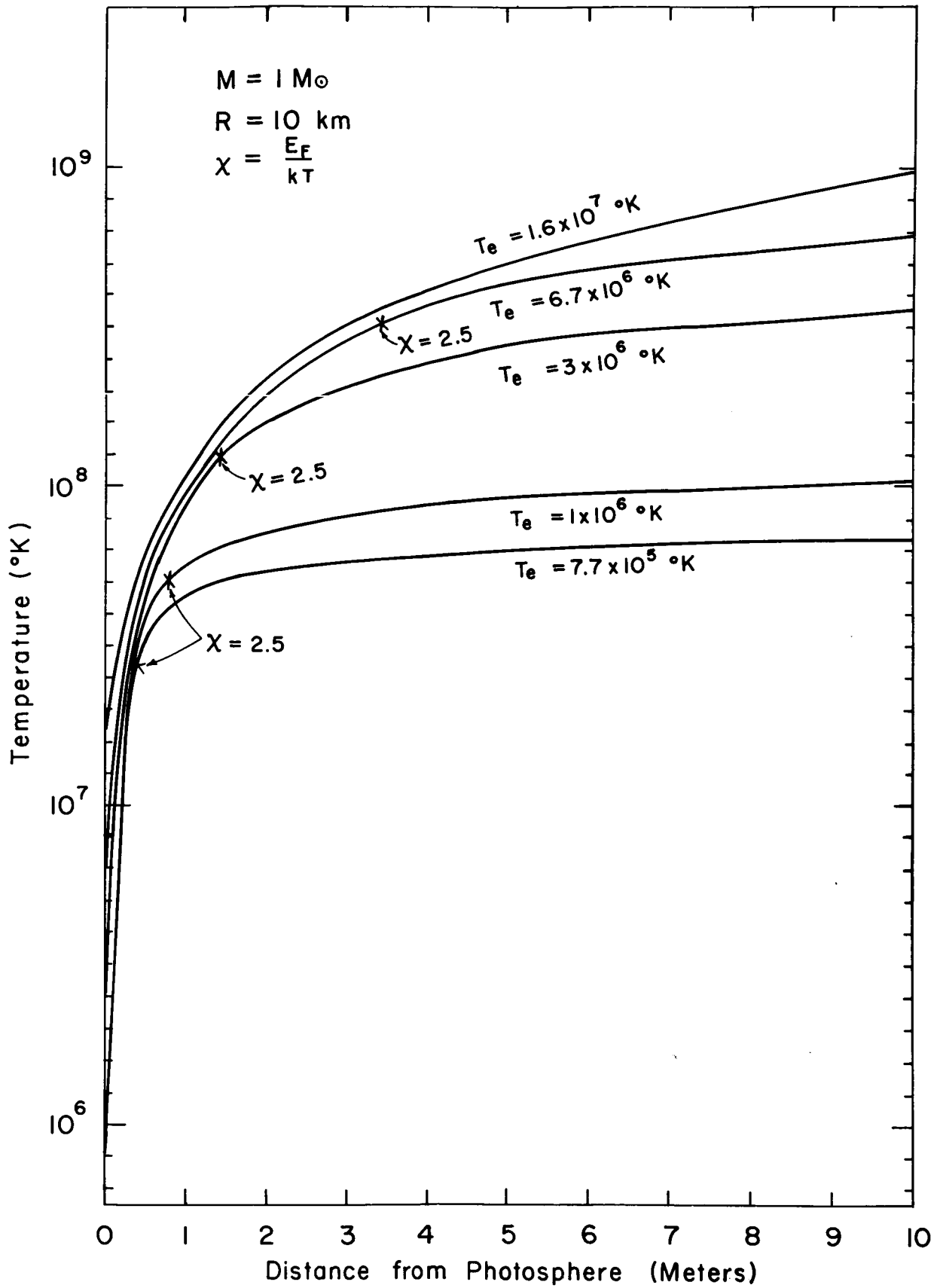


Figure 3

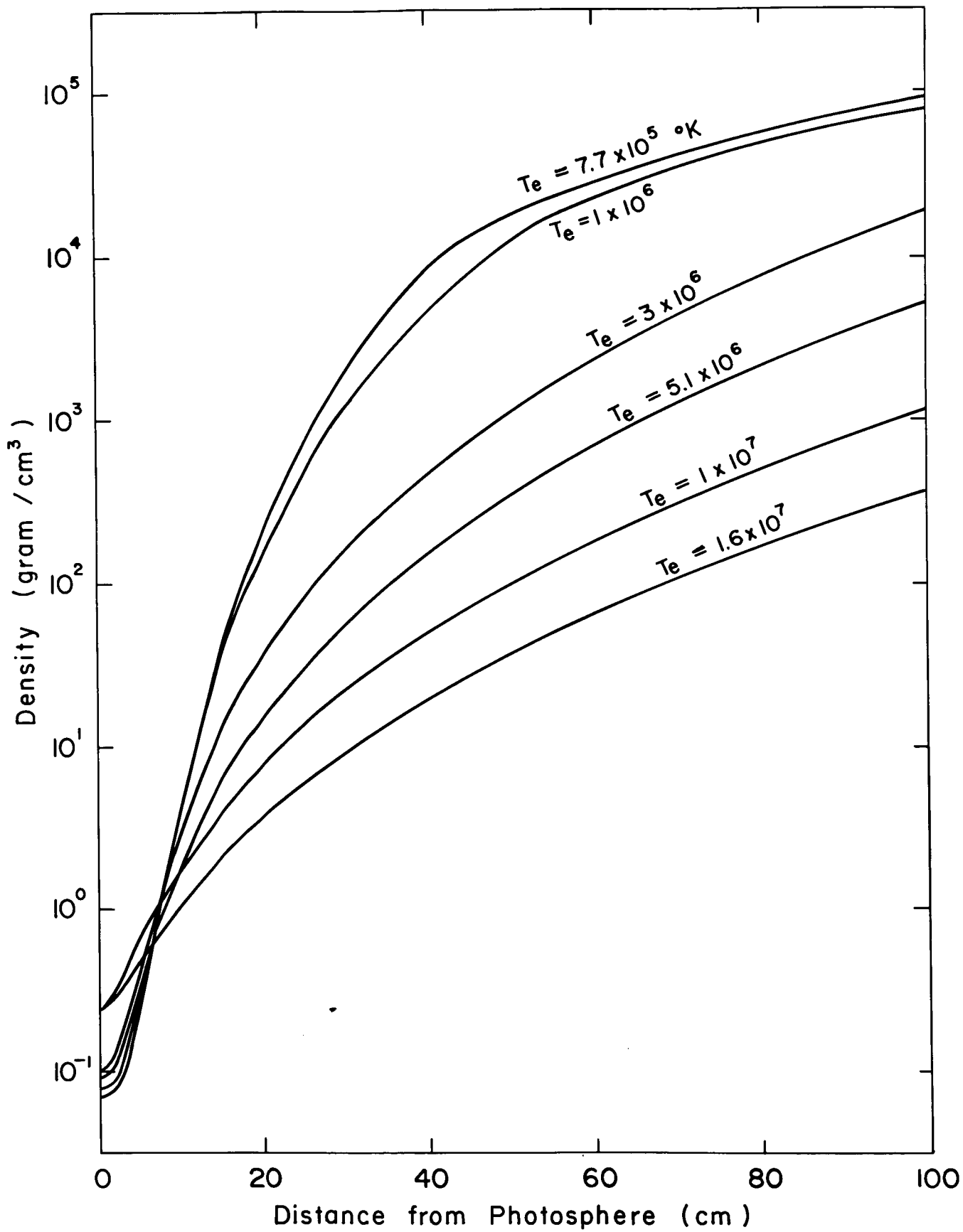


Figure 4

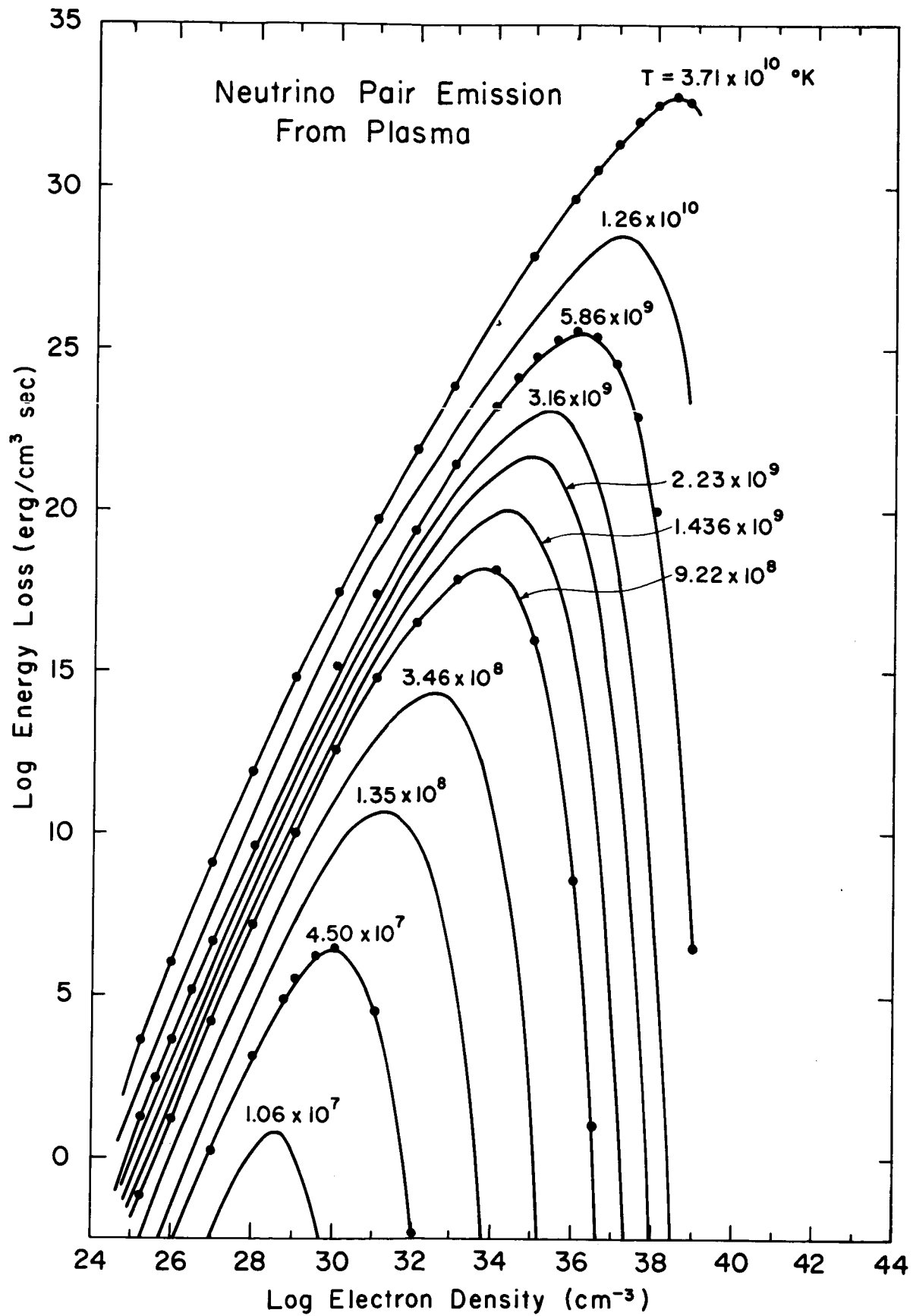


Figure 5

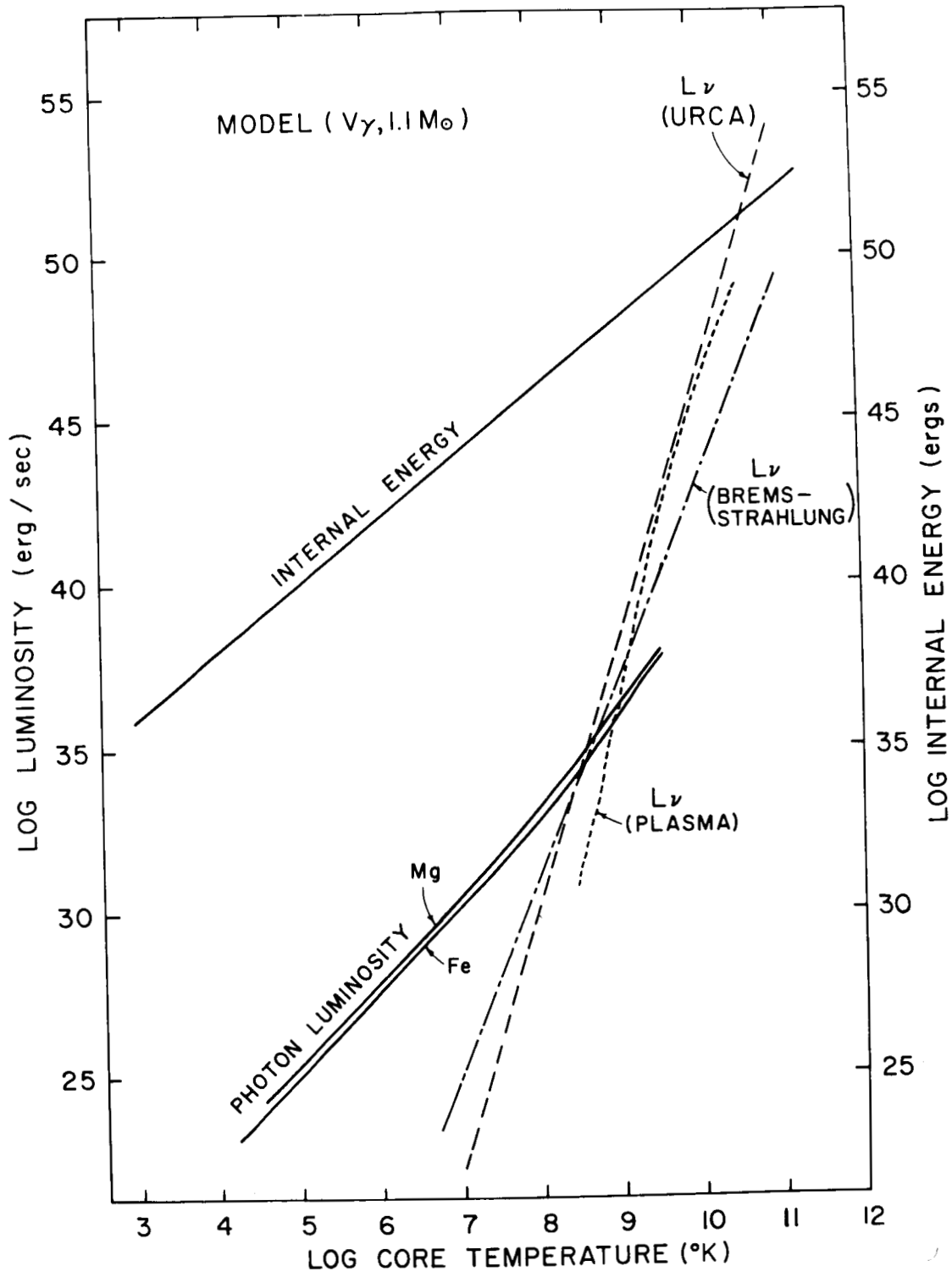


Figure 6

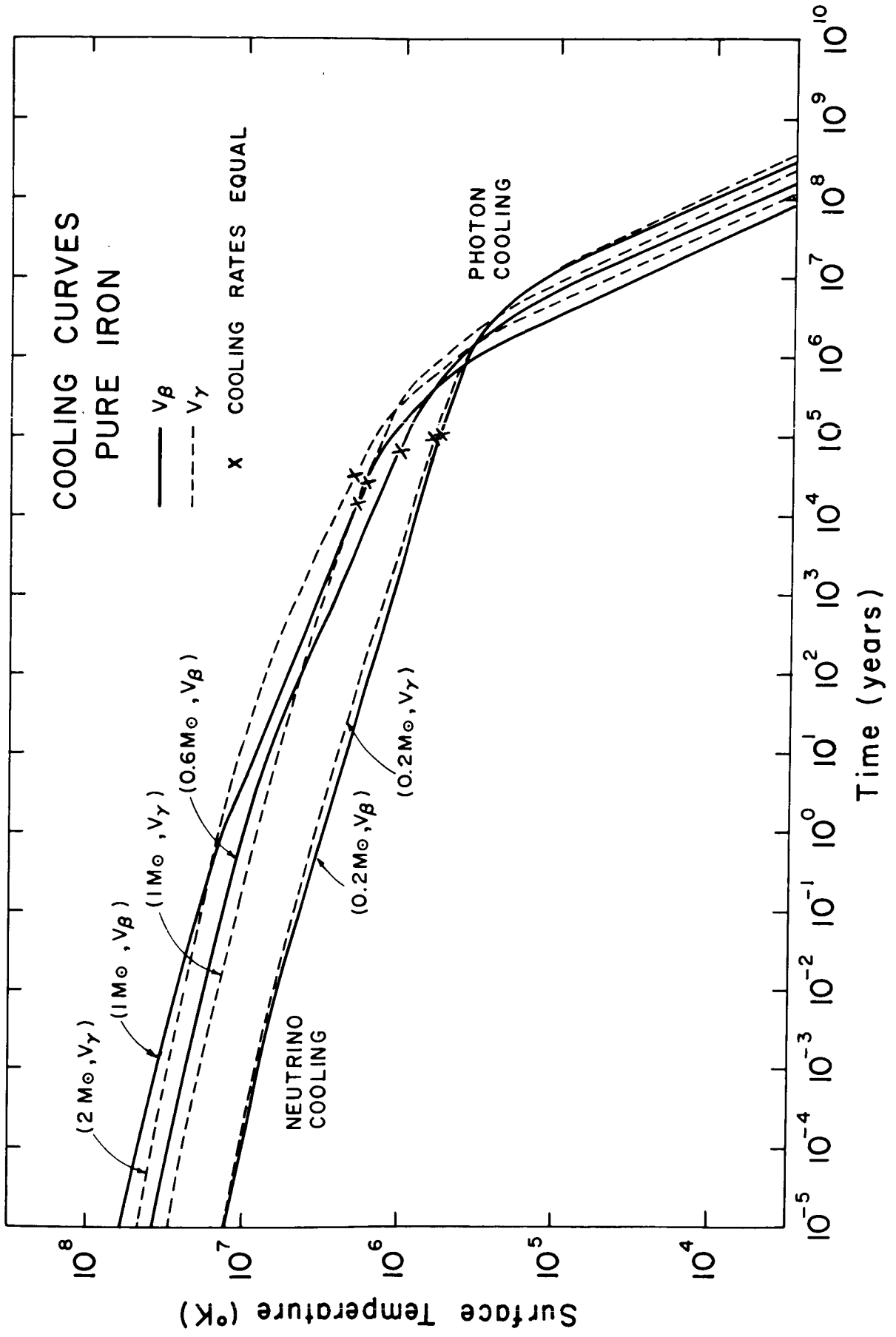


Figure 7

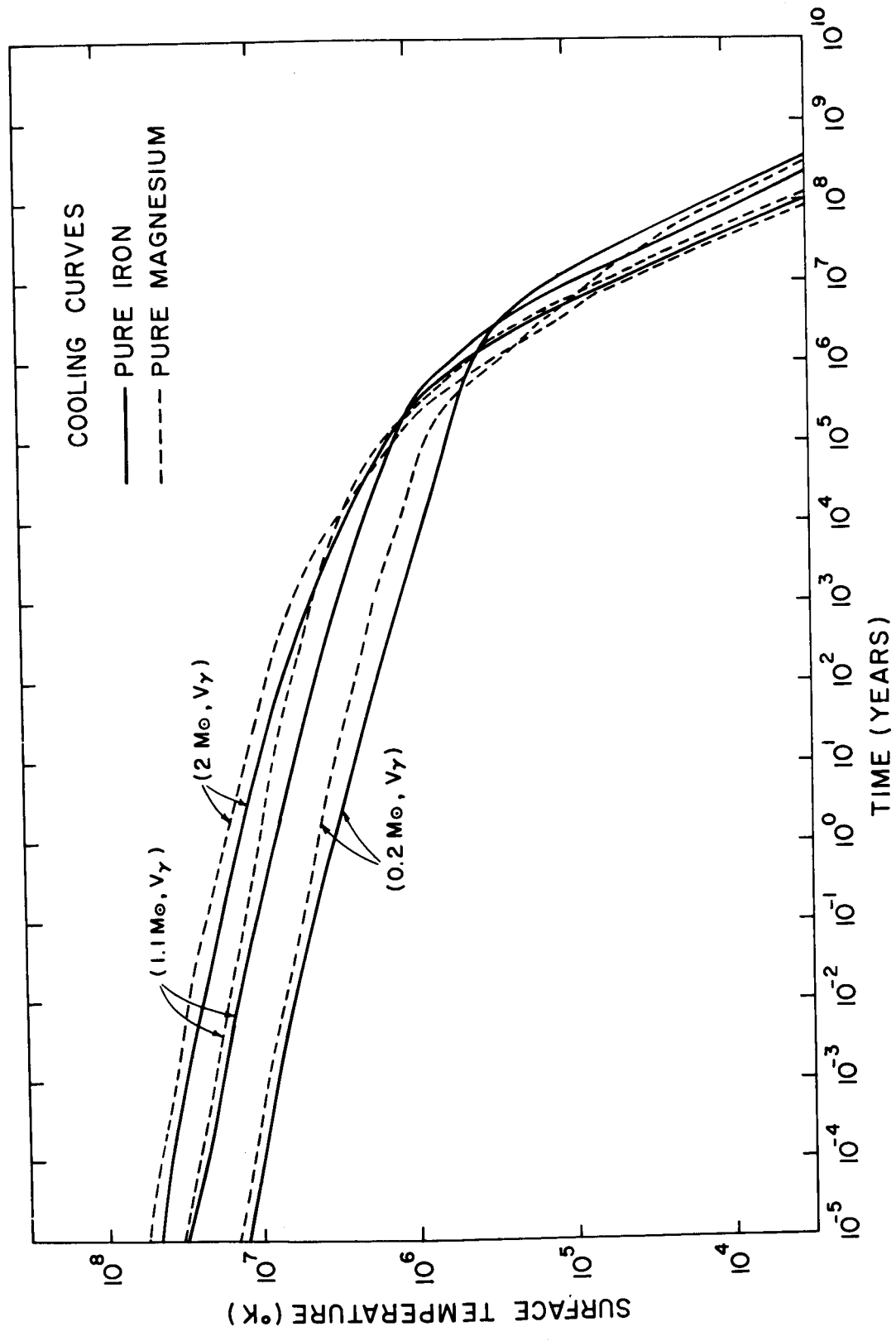


Figure 8

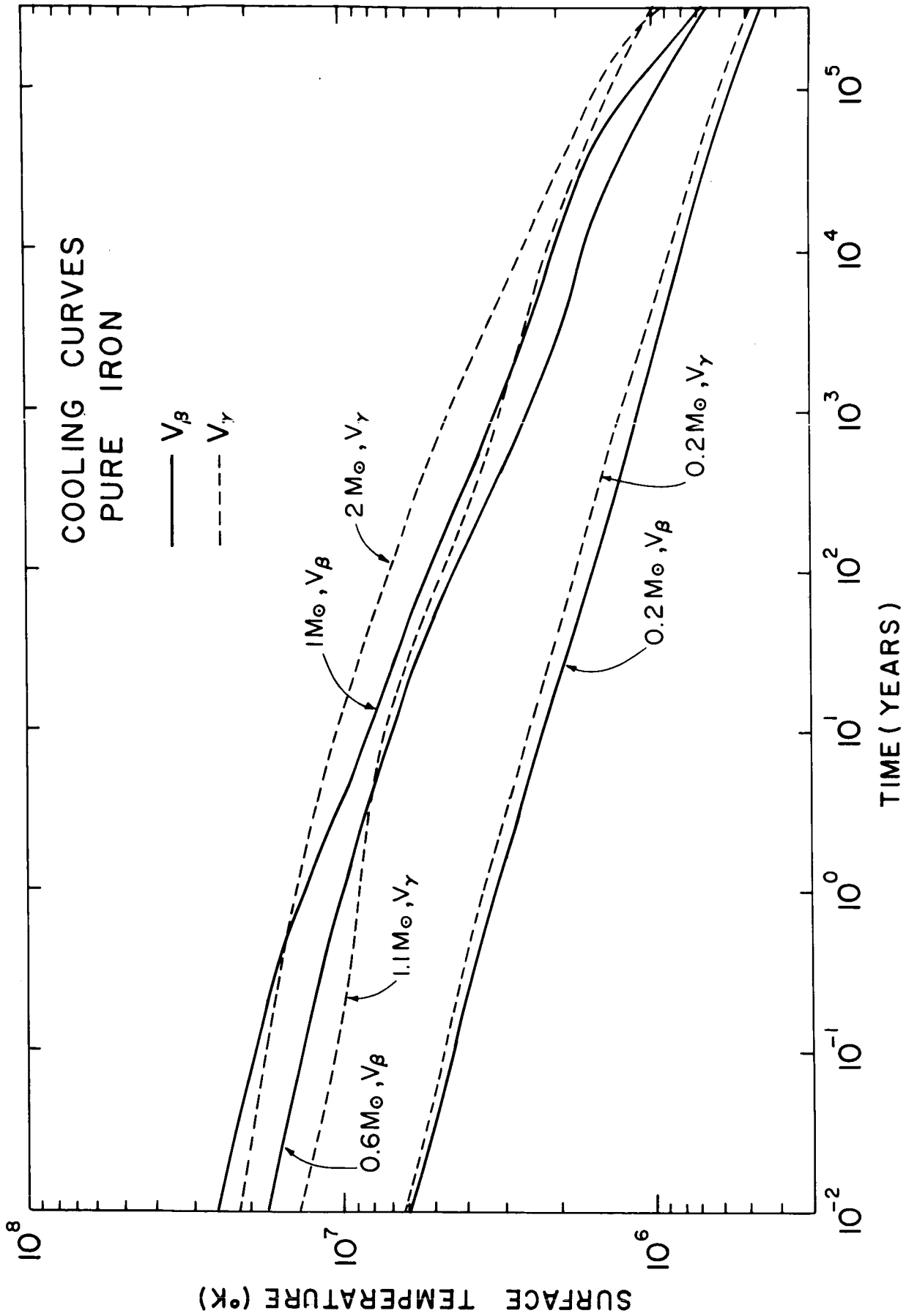


Figure 9

~~3693~~
~~10/2/67~~

10/2/67
3693
10/2/67